Q. J. R. Meteorol. Soc. (2001), **127**, pp. 1731–1760

Relationship between singular vectors and transient features in the background flow

By C. A. REYNOLDS*, R. GELARO and J. D. DOYLE
Naval Research Laboratory, Monterey, USA

(Received 24 July 2000; revised 26 February 2001)

SUMMARY

The relationships between singular vectors (SVs) and transient features in the background flow are examined through both composite techniques and case-studies. The SVs are derived using the NOGAPS forward and adjoint tangent models based on 48-hour forecasts during the NORPEX period. Composite results and case-studies both reveal significant spatial relationships between the SVs and transient features in the background flow. The SV perturbations often occur below distinctive high potential-vorticity (PV) features in the middle-to-upper troposphere. Case-studies reveal that the SVs propagate upward rapidly and have an impact on these PV features through the end of the optimization interval. In order to investigate how these small, initial perturbations have such a large impact on future development, the relationship between SVs and the quasi-geostrophic forcing is examined through the use of Q-vectors. The SV perturbations, while scaled to have a very small impact on the temperature and wind fields, have a very large impact on the mid-tropospheric Q-vectors. In contrast, the impact of the SV on the Q-vectors is negligible when added to an analysis field for which it is not optimal (e.g. the analysis field from another day). These findings establish a significant relationship between the SV perturbations and dynamically active regions in the middle troposphere, and point toward an integral link between SVs and upper-level PV precursors in synoptic development.

KEYWORDS: Potential vorticity Q-vectors

1. INTRODUCTION

The leading singular vectors (SVs) represent the fastest-growing perturbations (in a tangent linear sense) to a given trajectory, measured by a specified norm (Molteni and Palmer 1993; Buizza and Palmer 1995). As pointed out by Farrell (1982), non-modal perturbations can grow significantly faster than normal-mode perturbations for a finite period of time. As perturbations that produce optimal finite-time growth, the leading SVs lend themselves to many different applications. SVs have been used for predictability studies (Lorenz 1965; Farrell 1990; Molteni and Palmer 1993; Ehrendorfer and Errico 1995), they are being used to generate initial perturbations in the European Centre for Medium-Range Weather Forecasts (ECMWF) ensemble prediction system (Molteni *et al.* 1996), and they have been used to describe key analysis errors (Gelaro *et al.* 1998) in a manner similar to adjoint sensitivity (Rabier *et al.* 1996). Another natural application for SVs is targeted observations (Palmer *et al.* 1998), as successfully demonstrated in recent targeted field experiments such as the North Pacific EXperiment (NORPEX) and the Fronts and Atlantic Storm-Track EXperiment (FASTEX) (Bergot 1999; Gelaro *et al.* 1999; Langland *et al.* 1999; Buizza and Montani 1999; Gelaro *et al.* 2000). In this study, total energy SVs are related to transient features in the background flow, with particular emphasis on the background potential-vorticity (PV) field.

In complex time-dependent flows, both the structure and location of a perturbation determine its growth rate. The structures of the leading SVs have been examined in several studies using both simple and complex models. In both simple barotropic and baroclinic models, optimally growing perturbations exhibit an initial up-shear tilt, and extract energy from the mean flow as they are untilted by it (Farrell 1988, 1989; Lacarra and Talagrand 1988; Borges and Hartmann 1992). The leading SVs produced using primitive-equation models share many characteristics with the SVs from simple models

* Corresponding author: Naval Research Laboratory, 7 Grace Hopper Ave., Monterey, CA 93943-5502, USA.
e-mail: reynolds@nrlmry.navy.mil

Report Documentation Page

Form Approved
OMB No. 0704-0188

1. REPORT DATE	2. REPORT TYPE	3. DATES COVERED
26 FEB 2001		**00-00-2001 to 00-00-2001**

4. TITLE AND SUBTITLE	5a. CONTRACT NUMBER
Relationship between singular vectors and transient features in the background flow	5b. GRANT NUMBER
	5c. PROGRAM ELEMENT NUMBER
6. AUTHOR(S)	5d. PROJECT NUMBER
	5e. TASK NUMBER
	5f. WORK UNIT NUMBER
7. PERFORMING ORGANIZATION NAME(S) AND ADDRESS(ES) **Naval Research Laboratory,7 Grace Hopper Ave., Stop 2 ,Monterey,CA,93943-5502**	8. PERFORMING ORGANIZATION REPORT NUMBER
9. SPONSORING/MONITORING AGENCY NAME(S) AND ADDRESS(ES)	10. SPONSOR/MONITOR'S ACRONYM(S)
	11. SPONSOR/MONITOR'S REPORT NUMBER(S)

12. DISTRIBUTION/AVAILABILITY STATEMENT
Approved for public release; distribution unlimited

13. SUPPLEMENTARY NOTES

14. ABSTRACT

15. SUBJECT TERMS

16. SECURITY CLASSIFICATION OF:			17. LIMITATION OF ABSTRACT	18. NUMBER OF PAGES	19a. NAME OF RESPONSIBLE PERSON
a. REPORT	b. ABSTRACT	c. THIS PAGE			
unclassified	**unclassified**	**unclassified**	**Same as Report (SAR)**	**30**	

(Hartmann *et al.* 1995; Buizza and Palmer 1995; Buizza 1998). In more complex systems, leading SVs in a baroclinic environment typically have maxima in the middle-to-lower troposphere, near the steering level, and have fine-scale horizonntal and vertical structure. Buizza and Palmer (1995) explain how, in the case of an energetically amplifying Rossby wave packet, a phase tilt against the vertical shear leads to the group velocity being focused toward the jet core. This leads to an increase in the intrinsic frequency and therefore energy growth, while the propagation and refraction of the wave packet into the jet leads to a decrease in the tilt with time.

Recently, the physical mechanisms responsible for rapid perturbation growth have been examined using PV techniques in simple models. Badger and Hoskins (2001) use a simple two-dimensional quasi-geostrophic model to look at the development of fast-growing perturbations through a PV perspective. They find that optimal growth will be obtained by using a mid- or low-level PV anomaly with small vertical and horizontal scale. They note an initial period of rapid growth associated with the 'unshielding' of mid-tropospheric small-scale perturbations (Orr 1907; Farrell 1982). A rich vertical structure in the perturbation PV field is necessary for the PV unshielding and initial, rapid growth, which is proportional to the vertical shear. This initial fast-growth period is followed by a period of slower, sustained growth due to the coupling of interior PV anomalies and boundary thermal anomalies. Their results explain certain aspects of SV evolution in the ECMWF model as described by Hoskins *et al.* (2000). For short optimization time intervals, the SVs are initially located in the middle troposphere and evolve to the upper troposphere. For longer optimization times, the SVs are initially located in the lower troposphere, induce near-surface perturbations, and develop secondary energy maxima near the surface at final time. Morgan (2001) has examined SV growth in the Eady model using both PV and Eliasen–Palm flux diagnostics. He finds that the interior PV anomalies tilted against the shear are of primary importance for perturbation growth. He classifies different stages of perturbation growth as well, similar to the results of Badger and Hoskins (2001). Initial growth is due to the superposition of interior PV anomalies (unshielding), followed by an intensification of the boundary thermal anomalies induced by the internal PV anomalies and, finally, growth due to the mutual interaction of the boundary thermal anomalies.

Given the importance of unshielding during the initial, rapid growth phase, one might expect to find SVs located in regions of strong vertical shear. Buizza and Palmer (1995) examine a climatology of 36 h SVs produced using the ECMWF model for different seasons, and find a close correspondence between the location of the initial-time SVs and the seasonally averaged Eady index of baroclinic instability (Lindzen and Farrell 1980; Hoskins and Valdes 1990). They also find a close proximity between initial-time leading SVs and Eady growth-rate maxima in four case-studies examined. It should be noted that the amplification rates for the SVs are much larger than those indicated by the Eady index. Adjoint studies of developing cyclones also document large sensitivity in regions of strong vertical shear (e.g. Errico and Vukicevic 1992; Langland *et al.* 1995). Consistent with the mid to low-level location of initial-time SVs and adjoint sensitivity, recent studies have shown that forecasts can be very sensitive to analysis increments in the middle-to-lower troposphere (e.g. Pouponneau *et al.* 1999; Gelaro *et al.* 2000; Hello *et al.* 2000).

The importance of low-level perturbations derived from SV and adjoint sensitivity analysis may appear to be inconsistent with one of the core paradigms of synoptic meteorology. This paradigm is the importance of upper-level precursors in cyclone development, as in 'type B' cyclogenesis described by Petterssen and Smebye (1971), and illustrated by the 'PV-thinking' arguments described by Hoskins *et al.* (1985).

Recent studies have shown that the evolution of synoptic-scale systems can be sensitive to upper-tropospheric PV features (e.g. Fehlmann and Davies 1997; Huo *et al.* 1999a,b; Demirtas and Thorpe 1999). Fehlmann and Davies point out that this is not necessarily a contradiction of SV results, but that the SVs may evolve rapidly into perturbations that have significant amplitude at the tropopause level. Indeed evolving SVs do exhibit rapid upward energy propagation (Gelaro *et al.* 1999, 2000). The recent simple-model results of Badger and Hoskins (2001) and Morgan (2001) suggest that the interaction between internal PV anomalies and surface thermal anomalies is an important part of SV evolution, but occurs after the initial fast-growth phase dominated by the PV unshielding.

In more complex systems, there is accumulating evidence of a relationship between SVs and the transient background PV features in many cases. Palmer *et al.* (1998) show a case-study where SVs optimized to grow for 48 h occur below the equatorward edge of an upper-level PV anomaly. However, for SVs optimized to grow for 96 h, no such horizontal collocation exists. They point out, of course, that errors can propagate as the group velocity of waves, faster than the Lagrangian advection of certain PV features. Gelaro *et al.* (1999) show examples of the leading SVs being collocated with large PV gradients associated with middle-tropospheric fronts during FASTEX for IOP* 17 and IOP 18. In an examination of one of these FASTEX cyclones, Morgan (2001) relates the SVs to 'PV-thinking' by noting that the SV perturbations appear to enhance the interaction between the tropopause PV disturbance and the near-surface thermal anomalies by amplifying the upper-tropospheric PV and lower-tropospheric thermal waves.

In this study, the relationships between SVs and transient features in the background flow, such as upper-level PV streamers, are examined using composite techniques and case-studies. One purpose of this study is to relate the SVs to more traditional measures of synoptic–dynamic activity. Toward this end, Q-vector diagnostics are used to examine the relationship between SVs and quasi-geostrophic forcing in the mid-troposphere, as well as the impact of the SVs on this forcing. The link between SVs and upper-level PV features that can serve as 'precursors' to cyclone development will also be investigated. Establishing these relationships may provide insight into the physical mechanisms that lead to fast perturbation growth. A brief discussion of pertinent theory and the method employed are presented in section 2. The composite analysis and case-study results are presented in sections 3 and 4, respectively. A summary and conclusions are given in section 5.

2. METHODOLOGY

For sufficiently small errors and short time-scales, the growth of perturbations is governed by the tangent linear equations of the model such that

$$\mathbf{L}\mathbf{x}_0 = \mathbf{x}_t \tag{1}$$

where $\mathbf{L}$ is the forward tangent propagator (tangent linear matrix) of the model, and $\mathbf{x}_0$ and $\mathbf{x}_t$ are the perturbation at the initial and future time, respectively. The SVs of $\mathbf{L}$ are the eigenvectors of $\mathbf{L}^*\mathbf{L}$, where $\mathbf{L}^*$ is the adjoint of $\mathbf{L}$ with respect to a specific metric. The SVs are actually calculated for $\mathbf{K}^{1/2}\mathbf{L}\mathbf{K}^{-1/2}$ where $\mathbf{K}$ is a matrix such that for a state vector $\mathbf{x}$, $\mathbf{x}^T\mathbf{K}\mathbf{x}$ gives the measure of perturbation growth, or metric (the superscript T denotes the transpose). $\mathbf{L}$ may be expressed in terms of SVs and singular values (see

* Intensive Observing Period.

Molteni and Palmer 1993) such that

$$\mathbf{K}^{1/2}\mathbf{L}\mathbf{K}^{-1/2}=\mathbf{V}_\mathbf{K}\mathbf{\Sigma}_\mathbf{k}\mathbf{U}_\mathbf{K}^\mathrm{T} \tag{2}$$

where $\mathbf{U}_\mathbf{K}$ ($\mathbf{V}_\mathbf{K}$) is a matrix with columns that are the initial-time (final-time) SVs of $\mathbf{K}^{1/2}\mathbf{L}\mathbf{K}^{-1/2}$, and $\mathbf{\Sigma}_\mathbf{K}$ is a diagonal matrix whose elements are the singular values of $\mathbf{K}^{1/2}\mathbf{L}\mathbf{K}^{-1/2}$, ranked in order of descending magnitude. The leading initial-time SV, $\mathbf{u}_1$, represents the fastest-growing perturbation to the specific trajectory considered, which evolves into $\mathbf{v}_1$ and has an amplification factor given by the first singular value. The metric used here is the total energy metric as described by Rosmond (1997).

In this study, the SVs are calculated based on a T79 nonlinear full-physics integration of the forecast model of the Navy Operational Global Atmospheric Prediction System (NOGAPS, Hogan and Brody 1993). The SVs are calculated using the Lanczos algorithm applied to the dry forward and adjoint tangent equations of NOGAPS (Rosmond 1997) at a T79L18 resolution. A local projection operator (Barkmeijer 1992; Buizza 1994) is employed to maximize final-time perturbation variance over the verification region 30°N–60°N, 150°W–120°W. A set of leading SVs is calculated once daily based on a 48-hour integration starting from 00 GMT during the NORPEX period from 14 January to 20 February 1998. The composite results are based on these 38 consecutive cases. A description of the SVs calculated for this period is given by Gelaro *et al.* (2000).

In order to examine the spatial relationships between the SVs and transient features in the background flow in a systematic manner, a composite technique is employed. First, the location of the SV perturbation maximum for a selected field at a specified level is found. The SV field and the background fields of PV, potential temperature (θ), and other quantities at all vertical levels, are horizontally translated to a new grid uniformly such that the SV maximum is located at the origin. These translated fields are then averaged over the 38 cases to produce the composites. Estimates of the significance of the composites are based on 100 random composites (i.e. composites corresponding to the same SV maximum locations but created with randomly ordered dates). A composite value is considered significant if it is larger (smaller) than the second largest (second smallest) random composite value.

3. Composite results

(*a*) *Time-averaged fields and temporal variability*

Time-averaged fields are presented to provide a comparison with the composite results. The fields in Figs. 1 and 2 are averaged over the 38 cases from the NORPEX period used in this study. Figure 1(a) shows the background 300 hPa PV and θ. The PV and θ fields are fairly zonally symmetric, with no strong east–west gradients over the Pacific basin. Figure 1(b) shows the time-averaged leading SV (SV1) vertically averaged total energy perturbation at initial time. Superimposed on this field are the 50 m s^{-1} contour of the 300 hPa zonal wind and the 1.0 day^{-1} contour of the Eady growth-rate index. Following Lindzen and Farrell (1980) and Hoskins and Valdes (1990), the Eady index, σ_E, is defined as:

$$\sigma_\mathrm{E}=0.31\frac{f}{N}\frac{\mathrm{d}v}{\mathrm{d}z} \tag{3}$$

where f is the Coriolis forces, v is the magnitude of the vector wind, and N is the Brunt–Väisälä frequency. Here, σ_E is calculated for the 300–1000 hPa layer based on the daily

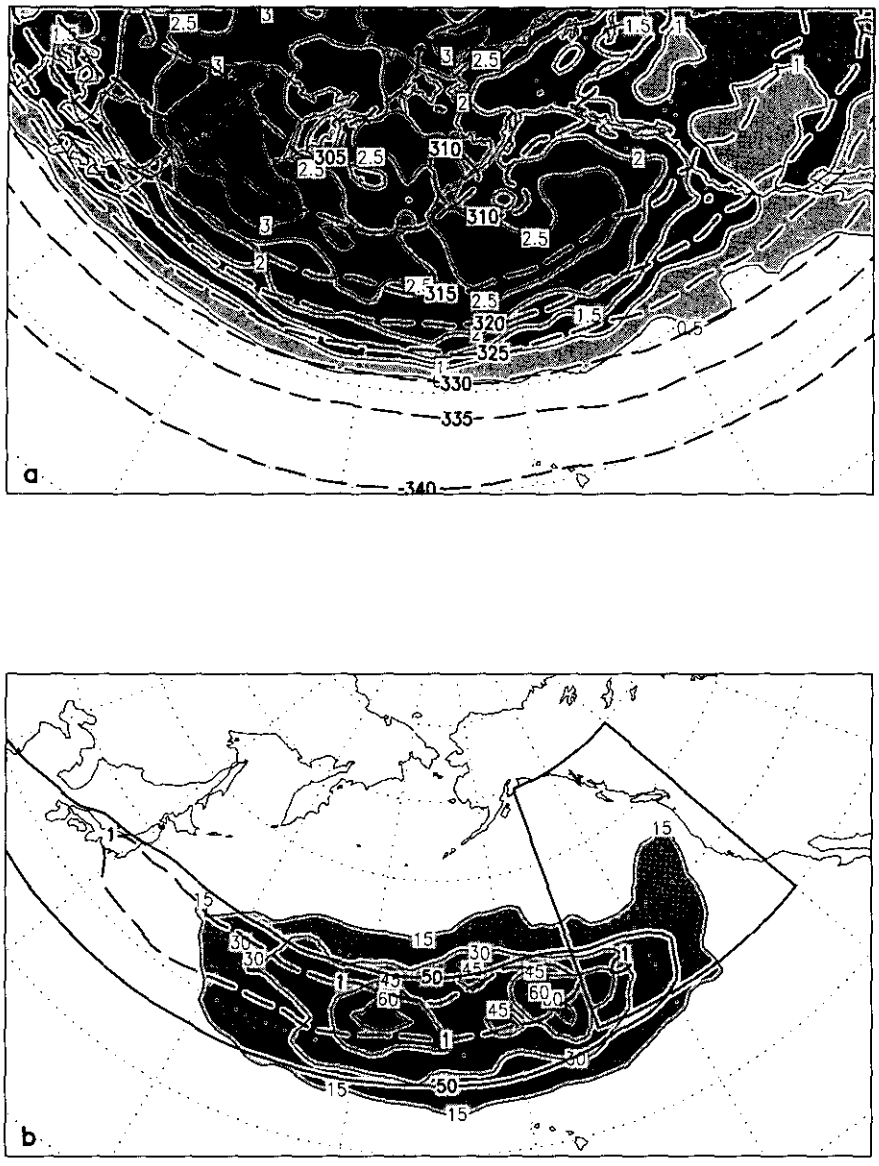

Figure 1. Time-averaged fields for (a) background 300 hPa potential vorticity (PV) (shaded, interval of 0.5 PV units) and background 300 hPa potential temperature (dashed contours, interval of 5 K), and (b) background 300 hPa zonal wind (solid contour at 50 m s^{-1}), Eady growth-rate index (dashed contour at 1.0 day^{-1}), and the leading singular vector (SV1) vertically averaged total energy (shaded, contour interval of 15 J kg^{-1}). The area of the local projection operator is denoted by the box.

analyses, then averaged for the 38 cases. The SV maxima occur at roughly the same latitude as the jet maximum and are also approximately collocated with regions of strong baroclinicity as indicated by the Eady growth-rate index. Of course, the longitudinal location of the SVs is modulated by the location of the local projection operator (given by the rectangular box), which defines the volume where final time energy is maximized.

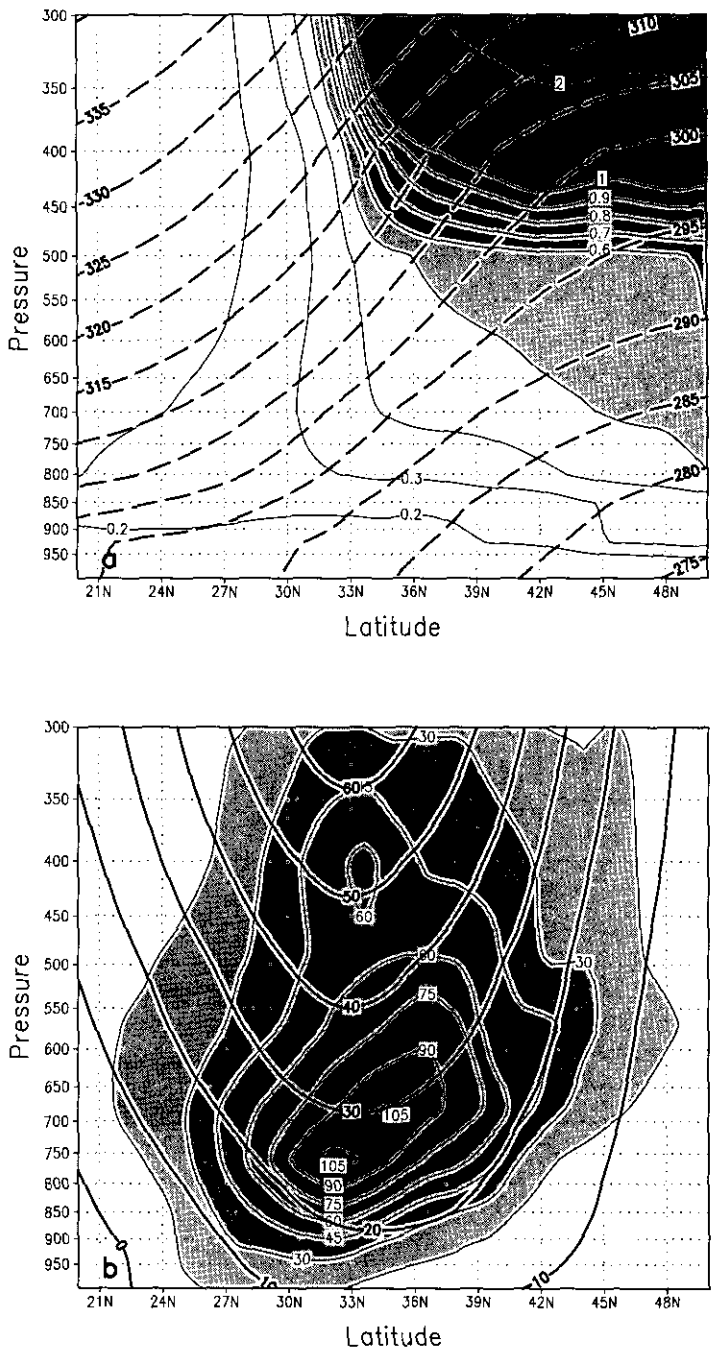

Figure 2. Pressure–latitude cross-sections of the time-averaged fields, averaged between 180° and 150°W for (a) background potential vorticity (PV) (contour interval of 0.1 PV units (PVU) below 1 PVU, shaded above 0.5 PVU) and background potential temperature (dashed contours, interval of 5 K), and (b) background zonal wind (solid contours, interval of 10 m s^{-1}), and the leading singular vector (SV1) total energy (shaded, contour interval of 15 J kg^{-1}).

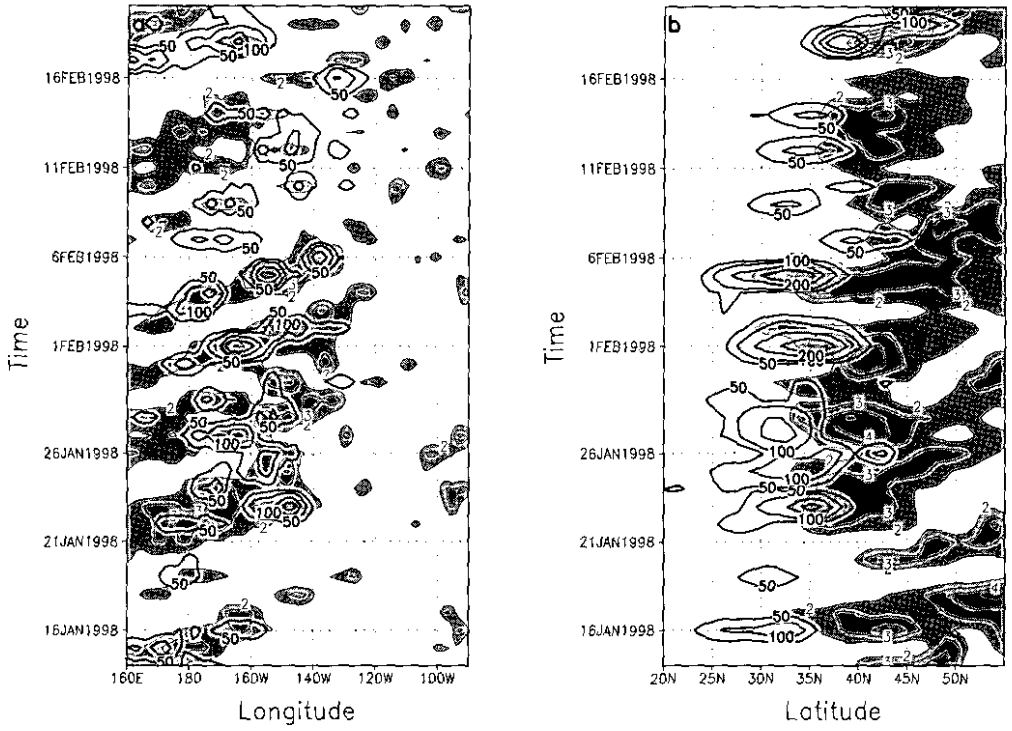

Figure 3. Time–longitude and time–latitude plots of the background 300 hPa potential vorticity (PV) (shaded, contour interval of 1 PV unit (PVU), contours below 2 PVU omitted) and the vertically averaged leading singular vector (SV1) total energy (thick contours, interval of 50 J kg^{-1}) for (a) from 160°E to 90°W, averaged from 30°N to 45°N; and (b) from 20°N to 55°N, averaged from 175°W to 150°W.

Figure 2 shows vertical cross-sections of these same fields averaged between 180° and 150°W (the longitudinal band where the SV perturbations are largest). The SV maximum is located in the middle-to-lower troposphere and the vertical axis tilts poleward with height (Fig. 2(b)). This maximum occurs beneath the upper-level jet and the upper-level latitudinal PV gradient.

Hovmüller diagrams can be useful for recognizing temporal relationships between the SV perturbations and features in the background flow. Figure 3(a) is a Hovmüller (time–longitude) diagram of the background 300 hPa PV and the vertically averaged SV1 total energy averaged from 30°N–45°N. Figure 3(b) shows a time–latitude plot of the same fields averaged from 175°W–150°W. The background PV and the SV perturbations in Fig.3(a) both exhibit an eastward propagation, and are often, but not always, collocated. There also appears to be a relationship between the PV and SV maxima in Fig. 3(b), with the low-level SV maxima often occurring equatorward of the upper-level PV maxima. The background lower-tropospheric PV (not shown) does not appear to exhibit a significant relationship with the low-level SVs.

A subjective examination of the 38-day time series also supports the existence of a spatial relationship between the low-level SVs and features in the background upper-level PV field. As an example, the 300 hPa PV for a six-day period from 22 to 27 January 1998 is plotted in Fig. 4. Also plotted is the vertically averaged total energy perturbation for SV1 from each day. The SV perturbation often occurs below the equatorward edge of an upper-level PV feature. This is consistent with the case-studies by Palmer *et al.*

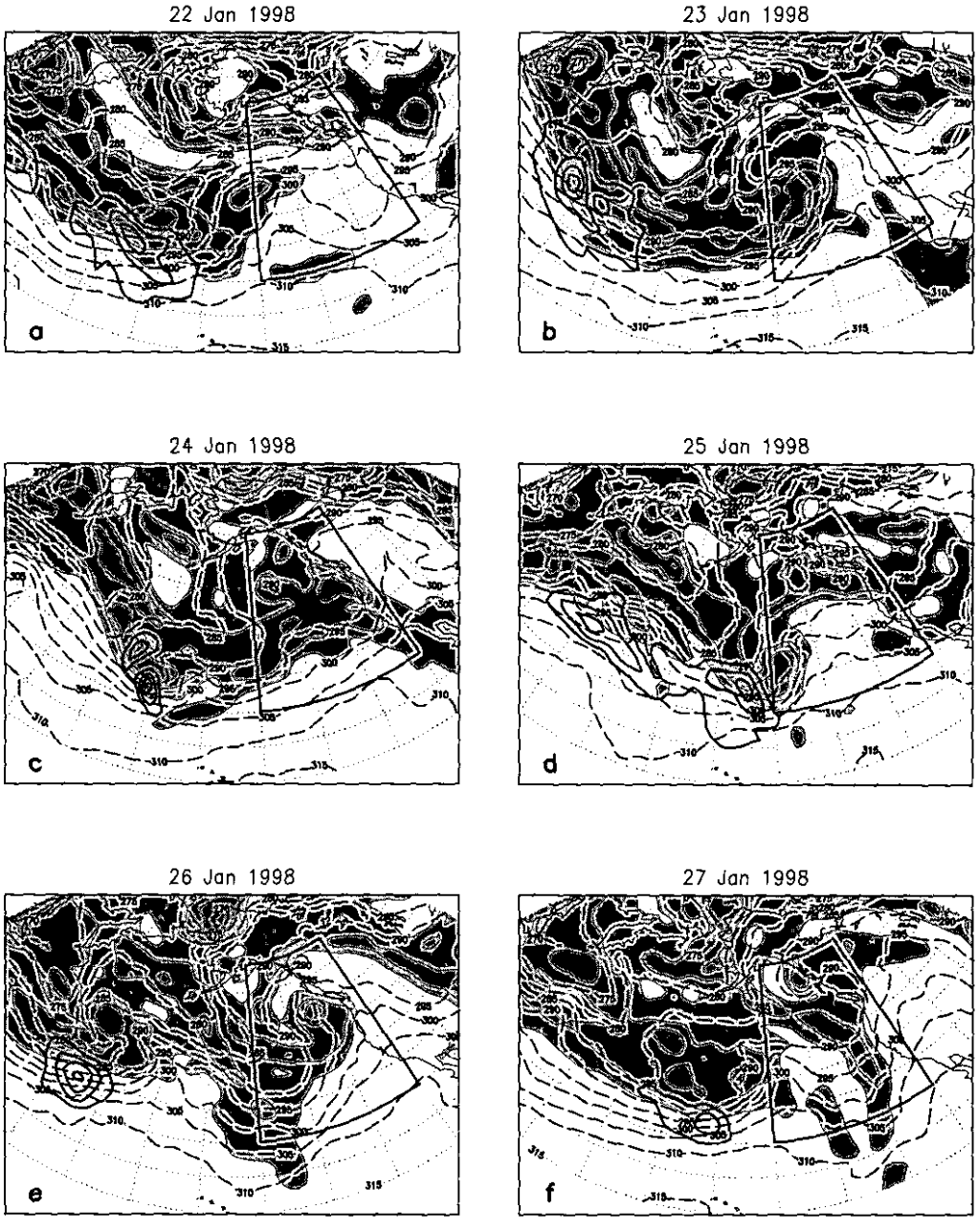

Figure 4. Background 300 hPa potential vorticity (PV) (shaded, contours at 2, 3, and 5 PV units) and background 700 hPa potential temperature (dashed contours, interval of 5 K) for six consecutive days (22 to 27 January 1998). The vertically averaged leading singular vector (SV1) total energy is denoted by the thick solid contours (interval of 50 J kg^{-1}). The area of the local projection operator is denoted by the box in each panel.

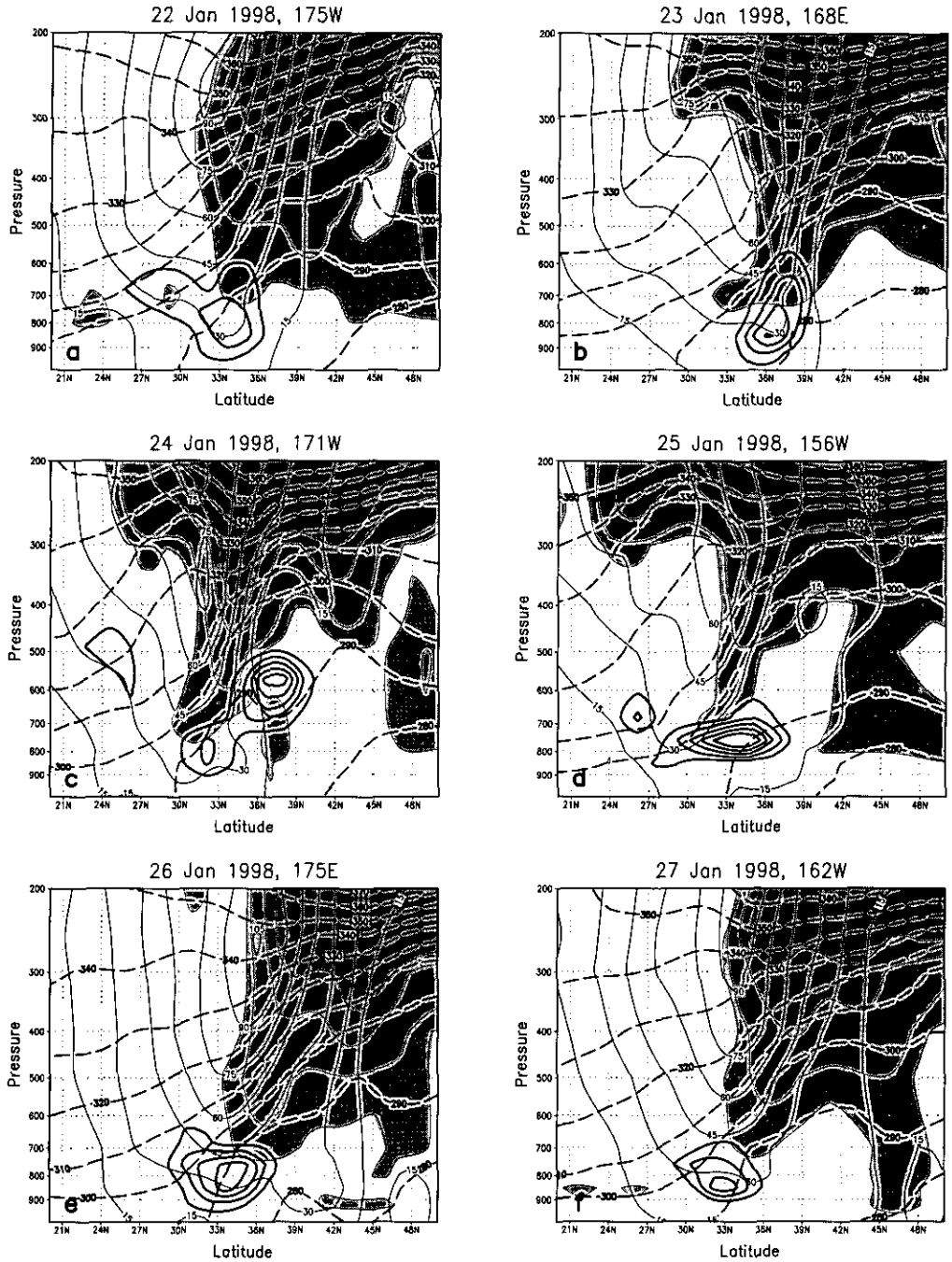

Figure 5. Same as Fig. 4, but vertical cross-sections as a function of latitude. The cross-sections are taken at the longitude of the singular vector (SV) perturbation maximum. Background potential vorticity (PV) is shaded with contours at 0.5, 1, 3, and 5 PV units. Background potential temperature is indicated by the dashed contours, (interval of 10 K). Background zonal wind is indicated by the thin solid contours, (interval of 15 m s^{-1}). The leading singular vector (SV1) total energy is indicated by the thick solid contours (interval of 200 J kg^{-1}).

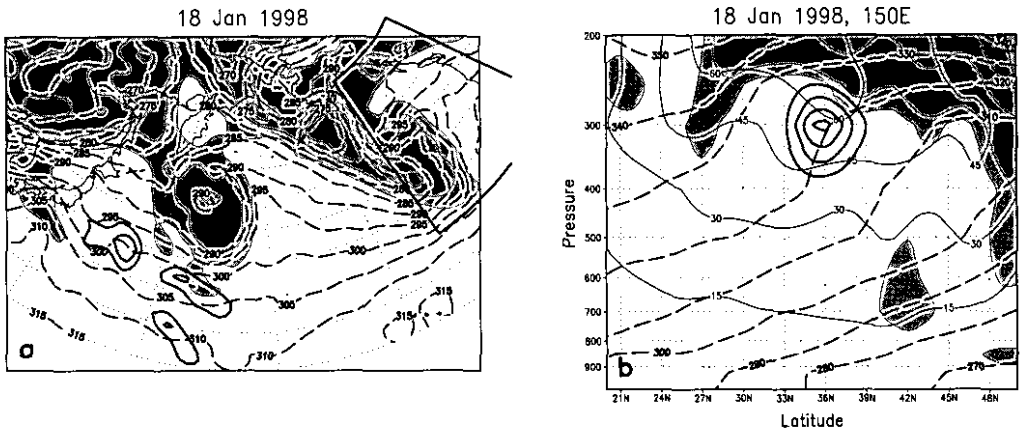

Figure 6. Same as Fig. 4(a) and Fig. 5(a), but for 18 January 1998.

(1998), Gelaro *et al.* (1999) and Morgan (2001). The background 700 hPa θ is also included in these figure panels. The SVs occur in regions of relatively large mid-level thermal gradients (and enhanced vertical shear, not shown). The relationships seen in this subset are representative of those found in the entire time series. Subjective evaluation indicates that the leading SV maxima are located beneath distinctive upper-level high-PV features approximately 80% of the time. During the other 20%, the initial-time SVs are either located at upper levels, or are located at low levels, but not below distinctive high-PV features.

Figure 5 shows pressure–latitude cross-sections corresponding to the panels in Fig. 4. The cross-section fields are centred on the longitude of the SV perturbation maximum. The background wind speed is shown in addition to the background θ and PV fields. There is a fair amount of variability in the shape of the SV perturbations and their exact relationship to features in the background PV field. However, the maximum SV perturbations often occur below, and sometimes just poleward of, an intrusion of high-PV air into the troposphere. Likewise, the SVs appear below the centre or north flank of an upper-level jet. These PV features, jets, and thermal gradients are similar to those exhibited by upper-level PV fronts, as in, for example, Davies and Rossa (1998) and Shapiro *et al.* (1987). The SVs usually occur in the vicinity of a relatively tight thermal gradient and strong vertical wind shear in the middle troposphere (though not necessarily near strong surface thermal gradients). It is not surprising to find the leading SVs in such baroclinic environments where a significant amount of background potential energy is available for conversion to perturbation energy.

For the NORPEX period, most of the leading SVs initially occur in the middle-to-lower troposphere; however, there are some exceptions. In seven out of the 38 cases, the SV1 initial-time maximum occurs at or above 400 hPa. Figure 6 illustrates one such exception, from 18 January. In this case, the SV maximum occurs at 300 hPa, and is located south and west of an upper-level trough in a region of relatively low-PV air. The vertical shear and horizontal temperature gradients at middle and lower levels are much weaker than in the cases shown in Fig. 5. The evolution of this upper-level perturbation, as compared with a typical low-level SV, will be examined in section 4(b).

(b) *Low-level composite results*

In order to examine the spatial relationships between the SVs and transient features in the background flow in a more systematic manner, a composite technique is employed. The composites are based on the SV1 total energy maximum at 760 hPa. This level is chosen because it is most often the location of the global SV maximum. Composites based on neighbouring pressure levels give very similar results. Other composites are discussed in the following subsection.

Figure 7(a) shows a vertical cross-section of the background PV and θ composites centred on the SV maximum. Note that the x-axis corresponds to the same latitudinal distance as that in the time-mean plots (Fig. 2). The PV composite area significant at the 98% level is shaded. The thin dashed contours indicate the SV composite. As suggested by Figs. 4 and 5, there is a significant anomaly of high-PV air above the SV maximum that slopes downward and equatorward from the upper troposphere. The SV maximum appears on the cold side of this feature. The mid-tropospheric PV and θ gradients are notably stronger in this composite than in the time-mean fields shown in Fig. 2. The composites suggest that the SVs occur in the vicinity of and beneath middle-to-upper-level frontal regions of strong PV and θ gradients.

The Q-vectors based on the geostrophic wind are used to diagnose regions of quasi-geostrophic forcing of vertical motion. Following Hoskins and Pedder (1980), the Q-vector is defined as:

$$\mathbf{Q} = \left[-\frac{\partial u_g}{\partial x}\frac{\partial \theta}{\partial x} - \frac{\partial v_g}{\partial x}\frac{\partial \theta}{\partial y}, -\frac{\partial u_g}{\partial y}\frac{\partial \theta}{\partial x} - \frac{\partial v_g}{\partial y}\frac{\partial \theta}{\partial y} \right] \tag{4}$$

where u_g and v_g are the zonal and meridional components, respectively, of the geostrophic wind. Upward (downward) motion is implied where $\mathbf{Q}$ is convergent (divergent) and Q-vectors crossing isotherms from cold to warm (warm to cold) air imply a thermally direct (indirect) circulation. The magnitude of the Q-vector is equivalent to the source term for the Sawyer–Eliassen secondary circulation (Sawyer 1956; Eliassen 1962), the significance of which is discussed in the review by Keyser and Shapiro (1986). Thus, the magnitude of the Q-vector is a measure of the transverse ageostrophic circulation associated with frontal zones. Q-vector diagnostics have been used to examine quasi-geostrophic forcing in a variety of midlatitude baroclinic systems (e.g. Boyle and Bosart 1986; Jusem and Atlas 1998; Martin 1999; Morgan 1999). Figure 7(b) shows the composites of the magnitude of the Q-vectors (shaded where significant), and the zonal wind. There is a statistically-significant relationship between the SVs and the Q-vectors. The largest Q-vector magnitude appears in the mid troposphere above the low-level SV maximum. Anomalously large low-level Q-vectors also appear equatorward of the SV maximum. Consistent with Figs. 2 and 5, the SV maximum occurs below the north flank of an upper-level jet. Also note that the strength of the upper-level jet and the horizontal and vertical shear are greater than in the time-mean fields (Fig. 2(b)).

Similar composites have been calculated for SVs of higher index (i.e. slower growth). The composites for these SVs become less significant as the index of the SV increases. SVs with an index of 20 have an average 2-day amplification factor of 3, compared with an average amplification factor of 14 for SV1. Composites based on these slower-growing SVs indicate a much weaker relationship with features in the background fields and look very similar to the time-mean fields. Thus, perturbations that grow more rapidly are also more likely to be located in dynamically active regions characterized by strong thermal gradients and large vertical shear.

Figure 8 shows composites of background PV, θ and Q-vectors at 500 hPa, and PV at 300 hPa (shading indicates where these composites are significant at the 98% level).

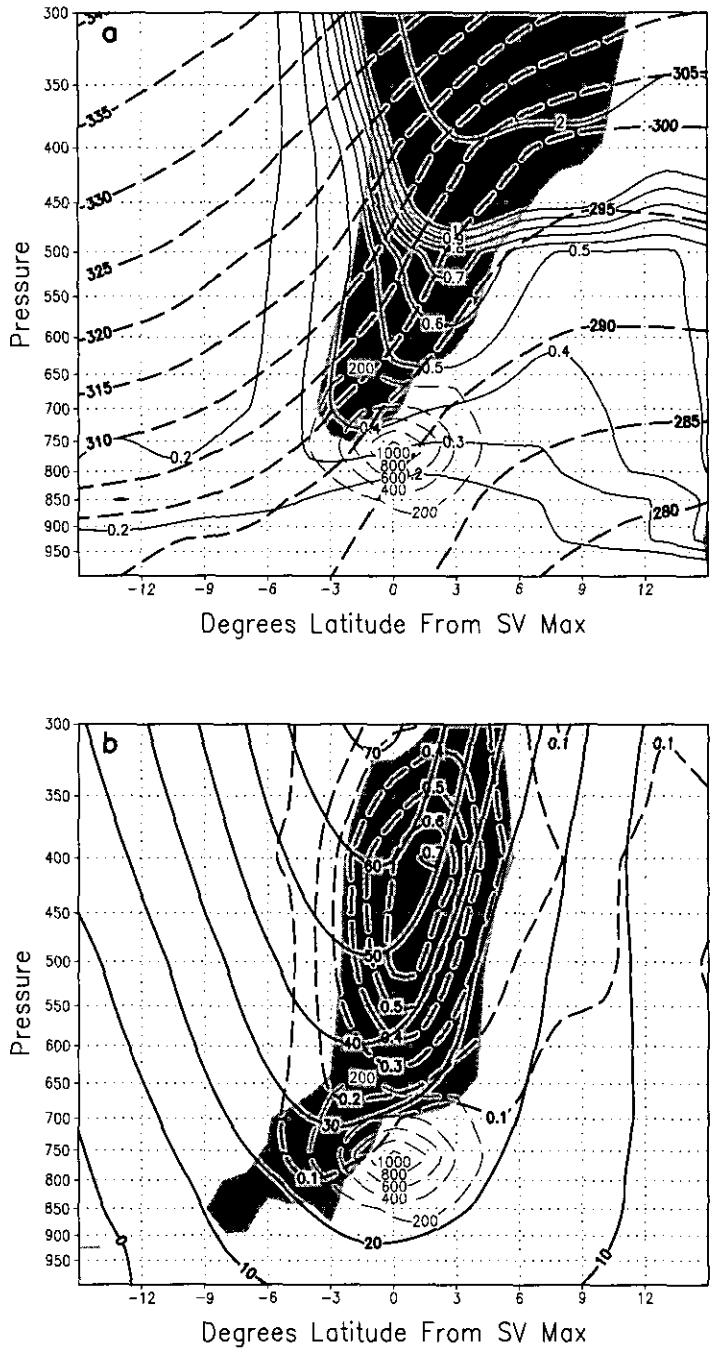

Figure 7. Pressure–latitude cross-section of the background composite fields based on the leading singular vector (SV1) low-level total energy maxima for (a) potential vorticity (PV) (solid contours, interval of 0.1 PV units (PVU) below 1 PVU), and potential temperature (thick dashed contours, interval of 5 K), and (b) magnitude of the Q-vectors (thick dashed contours, interval of 0.1×10^{-9} K m^{-1}s^{-1}) and zonal wind (thick solid contours, interval of 10 m s^{-1}). The composite SV perturbation is denoted in both panels by the thin dashed contours. Shading indicates the areas of 98% significance for the (a) PV and (b) Q-vector composites. The cross-sections are along the north–south axis taken through the SV composite maximum.

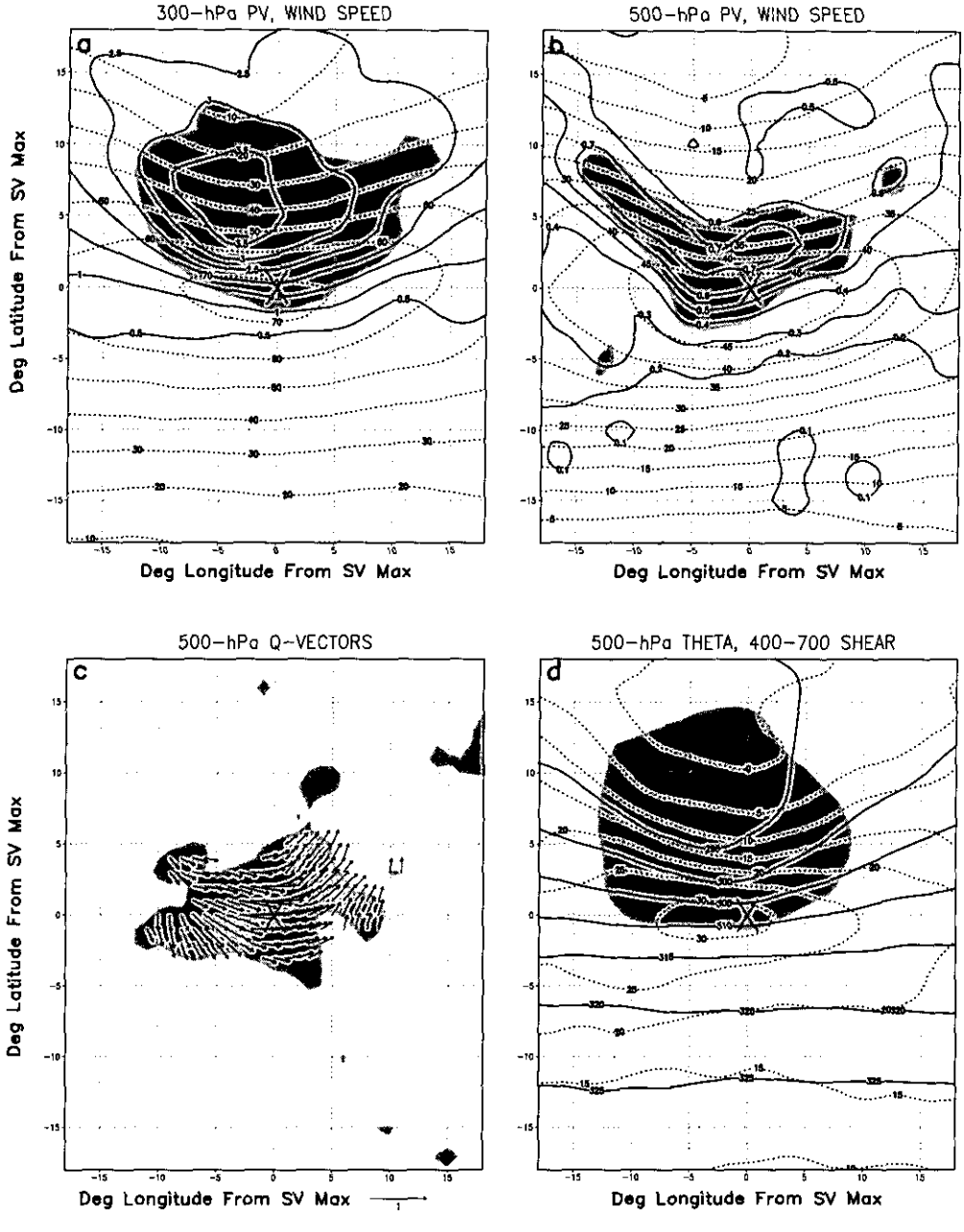

Figure 8. The background composites for (a) 300 hPa potential vorticity (PV) (solid contours, interval of 0.5 PV units (PVU)), (b) 500 hPa PV (solid contours, interval of 0.1 PVU), (c) 500 hPa Q-vectors (vector scale is 1×10^{-9} K m^{-1}s^{-1}), and (d) 500 hPa potential temperature (θ) (solid contours, interval of 5 K). The shading in each panel indicates where the composites are significant at the 98% level. The 300 hPa and 500 hPa wind speed composites (dotted contours) are superimposed on the PV fields (a) and (b). The 400 to 700 hPa vertical shear of the zonal wind composite (dotted contours, interval of 5 m s^{-1} per 300 hPa) is superimposed on the θ field (d). The 'X' denotes the location of the 760 hPa singular vector maximum.

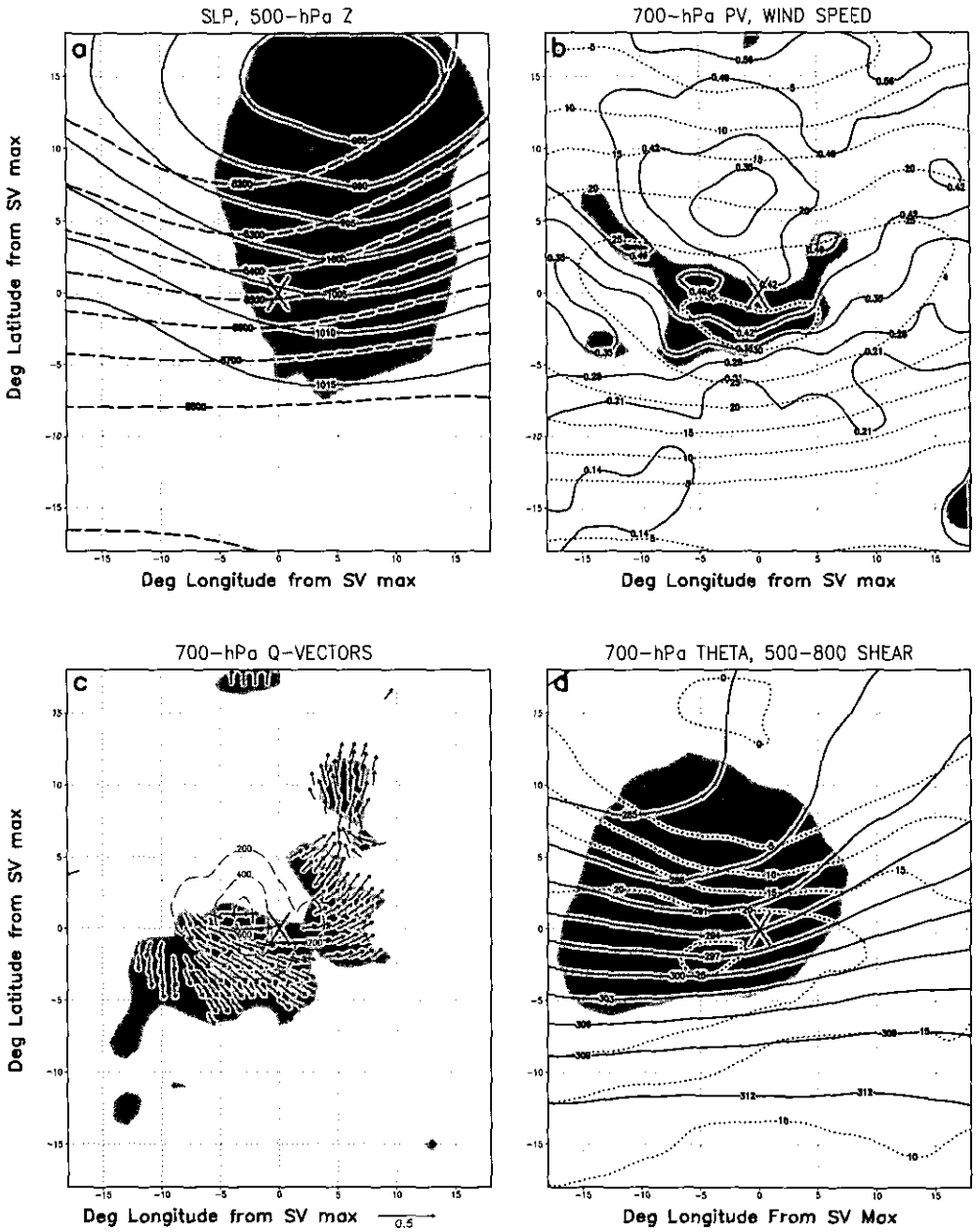

Figure 9. The background composites for (a) sea-level pressure (SLP) (solid contours, interval of 5 hPa), (b) 700 hPa potential vorticity (PV) (solid contours, interval of 0.07 PV units), (c) 700 hPa Q-vectors (vector scale is 0.5×10^{-9} K m^{-1}s^{-1}), and (d) 700 hPa potential temperature (θ) (solid contours, interval of 3 K). The shading in each panel indicates where the composites are significant at the 98% level. The 500 hPa geopotential height field (thick dashed contours) is superimposed on the SLP field (a). The 700 hPa wind speed composite (dotted contours) is superimposed on the PV field (b). The 500 to 800 hPa vertical shear of the zonal wind composite (dotted contours, interval of 5 m s^{-1} per 300 hPa) is superimposed on the θ field (d). The singular vector composite (thin dashed contours) is superimposed on the Q-vector field (c).

Composite wind speed fields are superimposed on the PV fields and the vertical shear of the zonal wind is superimposed on the θ field. The 'X' in the middle of each panel gives the position of the 760 hPa SV total energy maximum. On average, the lower-level SVs are located to the south and slightly east of an upper-level trough, below a localized jet maximum embedded in an enhanced baroclinic zone of strong horizontal thermal gradients and vertical shear. Note the complex structure in the 500 hPa PV field, featuring a relatively thin, elongated structure that appears similar to a PV streamer (Appenzeller and Davis 1992). The low-level SV maximum is positioned at the base and slightly to the east of this feature. The zonal wind composites also indicate that SVs tend to occur in regions of enhanced horizontal shear, and composites based on horizontal deformation (not shown) confirm this. There are also significant signals in the θ and Q-vector fields.

Figure 9 shows background PV, θ and Q-vector composites at 700 hPa, as well as the sea-level pressure (SLP) composite. Shading denotes where these composites are significant. The 500 hPa geopotential height composite is superimposed on the SLP composite (Fig. 9(a)). The SVs are not collocated with SLP minima, but occur equatorward of the surface low-pressure centre. The westward phase tilt between the surface cyclone and the 500 hPa trough indicates that the SVs are associated with growing systems. As in Fig. 8, the wind speed composite is superimposed on the PV field and the vertical shear is superimposed on the θ field. At this level, anomalously high-PV air occurs equatorward of the SV maximum, although the composite signal is weaker. The SV total energy perturbation composite at 700 hPa is superimposed on the Q-vector composite (Fig. 9(c)). The west-north-westward displacement of this feature from the 760 hPa maximum denoted by the X illustrates the vertical tilt of the SVs. The Q-vectors appear to wrap around the southern and eastern side of the SV maximum. There is also a strong cold anomaly in the θ composite (Fig. 9(d)). It is evident that the SVs occur in regions of enhanced horizontal temperature gradients and vertical shear. The tilt of the perturbation against this vertical shear is indicative of baroclinic energy transfer from the background available potential energy to perturbation energy.

These composites establish a spatial relationship between the SVs and transient features in the background flow. Although the largest PV gradients occur at upper levels, and the SVs have their largest amplitude in the lower troposphere, there is still a clear relationship between the two. These results indicate that the SVs often occur at or below regions characterized by strong quasi-geostrophic forcing, PV intrusions, and deep vertical shear. The finding that SVs consistently occur below distinct PV features suggests a link between the SVs and upper-level PV precursors that can be important for synoptic development.

(*c*) *Additional composites*

All composite results presented above have been based on the SV1 total energy maximum at 760 hPa, the level where the SV maxima occur most often. Composites based on SV maxima at other middle-to-lower tropospheric levels yield very similar results. However, as pointed out previously, the leading SVs do not always have an initial-time maximum in the lower troposphere (they are found at or below 500 hPa in 31 cases and at or above 400 hPa in 7 cases). Removing the seven cases of what will be referred to as 'upper-level' SVs from the composite does not have a significant impact on the results (the composite features become a bit sharper and are significant over a slightly larger region). Compositing above the low-level maxima of only the seven upper-level SV cases yields composite fields that are not significantly different from the time-mean fields. Compositing about the upper-level maxima in these seven cases

actually shows the SVs to be found to the south of the upper-level PV gradient (these composites are less significant than the low-level composites). It should be noted that the upper-level SVs have corresponding singular values (amplification factors) that are, on average, similar to the singular values for the low-level SVs.

In general, no significant relationship is found between the amplification factor of the SVs and the level or latitude of the SVs. However, the western-most SVs have slightly larger amplification factors than the eastern-most SVs. The wide longitudinal band over which the SVs occur (Figs. 1 and 3) indicates large variability in the propagation distance between initial and final times. One might expect that SVs that propagate over large horizontal distances may have a different relationship with background features than SVs that propagate over small distances. However, composites based on initial SVs that occur to the west of the dateline and composites based on initial SVs that occur to the east of 160°W are both very similar to the composites based on all the leading SVs. This suggests no systematic difference between SVs based on their two-day propagation distance, at least during the relatively short (38-day) time-period considered here.

Temperature-based composites yield very similar results to the total energy composites because, at initial time, most of the perturbation energy lies in the perturbation mass field, rather than the wind field. Composites based on the vorticity maxima yield similar results, although the composite features are shifted poleward, reflecting that the vorticity perturbation maxima usually occur equatorward of the temperature perturbation maxima. Composites based on the location of the vertically averaged perturbations also yield similar, though less significant, results. In sharp contrast to the initial-time SVs, composites based on the evolved SVs do not yield any significant structures. This is probably due to the fact that, by final time, the perturbations are of the same spatial scale as features in the background flow, and may also reflect differences between perturbation phase speed and group speed propagation, as will be discussed in the next section.

4. Case-study results

(*a*) *Impact on quasi-geostrophic forcing*

Composites yield a coarse picture of the environment in which the SVs occur. A more detailed examination of a particular case is made in order to elucidate the fine-scale structures that are filtered out during the composite averaging. The first case examined, 24 January 1998, is chosen because of the typical structure of the SV and its relationship to the background PV features. The amplification factor of 13.7 for SV1 in this case is slightly below the average value for the entire time period.

Figure 10 shows the background PV for this date and the SV1 temperature perturbation at 500 hPa and a vertical cross-section at 171°W. The Q-vectors of the background field are also shown in Fig. 10(a), and the magnitude of these Q-vectors is shown in Fig. 10(b). A large negative SV temperature perturbation is aligned immediately along the north side of the PV anomaly, with a smaller positive temperature perturbation along the south-west side of this feature. The Q-vectors appear to wrap around the equatorward side of the negative lobe of the SV temperature perturbation. In the vertical cross-section there is a very close correspondence between the background PV and the SV, with the SV temperature perturbations occurring on the north side of the localized PV maxima. The maximum background PV and Q-vectors, as well as the SV temperature perturbations, all have a similar poleward tilt with height. The case-study bears a strong resemblance to the composite results (Fig. 7).

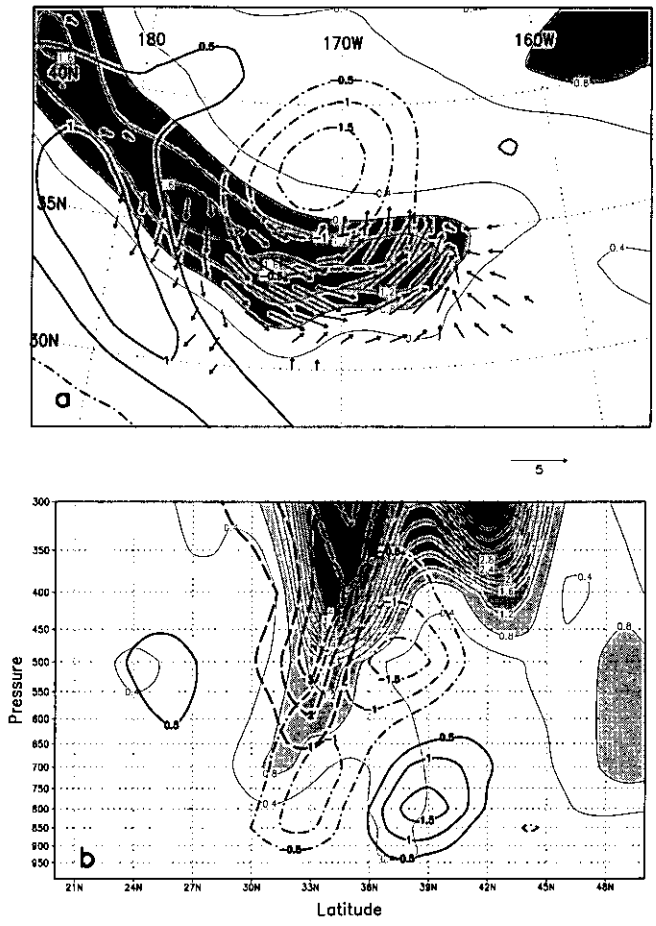

Figure 10. Case-study from 24 January 1998: (a) 500 hPa cross-section of background potential vorticity (PV) (shaded, contour interval of 0.4 PV units (PVU)) and Q-vectors (vector scale is 5×10^{-9} K m^{-1}s^{-1}), along with the leading singular vector (SV1) temperature perturbation (contour interval of 0.5 K, positive (negative) values denoted by solid (dot-dash) contours, zero contour omitted); and (b) pressure–latitude plot of the background PV (shaded, contour interval of 0.4 PVU up to 4.0 PVU), magnitude of the Q-vectors (thick dashed contours, interval of 1×10^{-9} K m^{-1}s^{-1}) and the SV1 temperature perturbation (contour interval of 0.5 K, positive (negative) values denoted by solid (dot-dash) contours, zero contour omitted) at 171°W.

The composite and case-study results show that SVs occur in regions of large quasi-geostrophic forcing. To investigate the impact of the SVs on this forcing, the SV perturbations are scaled and then added to or subtracted from the background field. The scaling factor used is consistent with the average projection of analysis differences onto the leading SVs (Gelaro *et al.* 2000). These perturbed fields are referred to as the positive and negative background fields, respectively. The scaled SV perturbations are relatively small (the maximum temperature perturbations are locally less than 1.8 K). The 500 hPa PV and θ for the positive and negative background fields are shown in Figs. 11(a) and 11(c), respectively. The 500 hPa Q-vectors and Q-vector divergence and the 400 to 700 hPa vertical shear of the zonal wind for the positive and negative background fields are shown in Figs. 11(b) and 11(d). The size of the initial-time mass- and wind-field perturbations are small enough such that it is difficult to distinguish

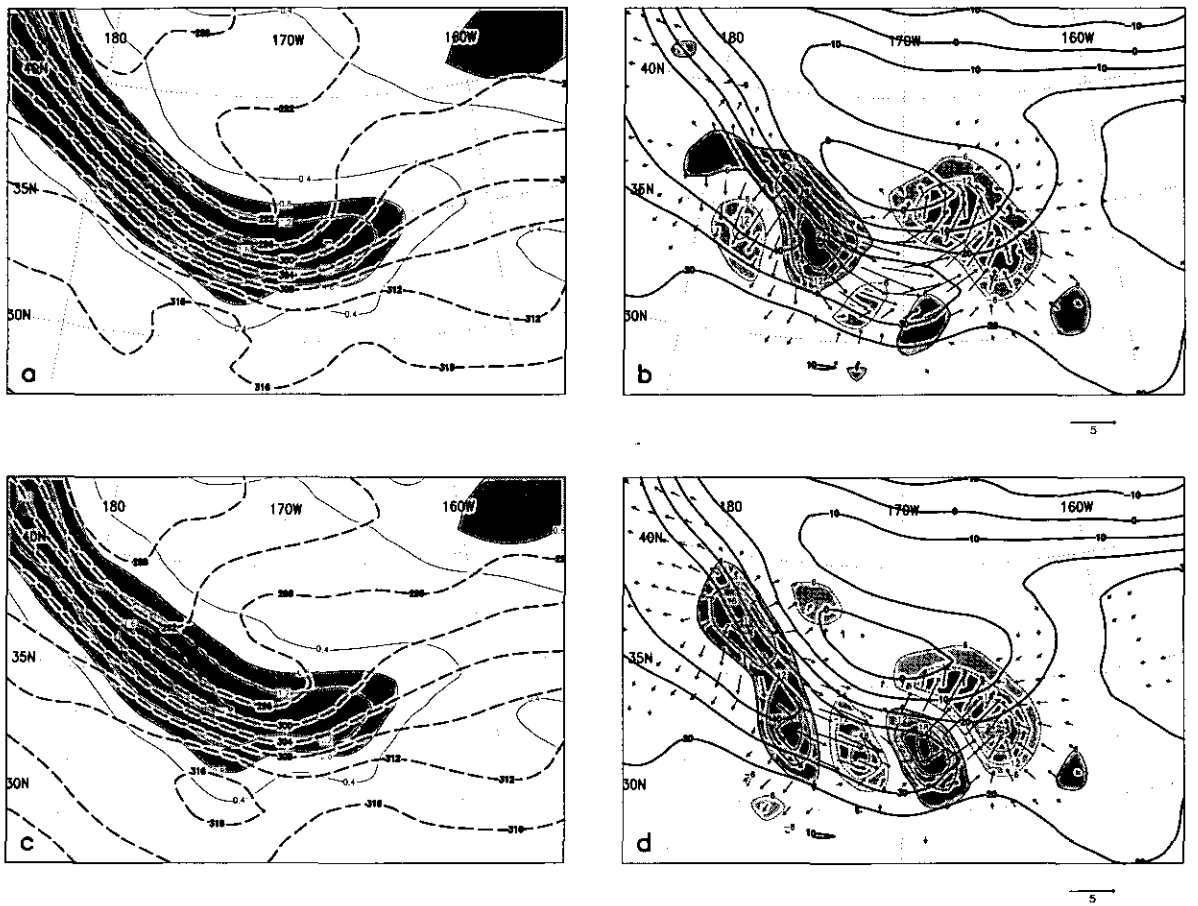

Figure 11. Case-study from 24 January 1998: 500 hPa potential vorticity (PV) (shaded, contour interval of 0.4 PV units) and potential temperature (dashed contours, interval of 4 K) for the (a) positive background and (c) negative background fields. The Q-vectors (vector scale of 5×10^{-9} K m^{-1}s^{-1}) and Q-vector divergence (shaded, contour interval of 6×10^{-15} K m^{-2}s^{-1} with zero contour omitted) for the (b) positive background and (d) negative background fields. The 400 to 700 hPa vertical shear of the zonal wind (solid contours, interval of 10 m s^{-1} per 300 hPa) for the (b) positive background and (d) negative background fields is also shown.

visually between the two PV and θ fields, although the θ gradient across the PV field is larger in the positive background case than in the negative background case. On the other hand, the differences in the Q-vector fields are obvious. The positive background field has stronger Q-vector divergence (and implied quasi-geostrophically-forced descent) at 34°N, 174°W than does the negative background field. The Q-vectors are largest in the vicinity of the large horizontal thermal gradients (which are also regions of large vertical wind shear). The occurrence of SVs in regions of enhanced vertical wind shear, and their tilt against that shear, enables them to tap the available potential energy of the background flow. There is a larger component of the Q-vectors across the isentropes in this vicinity in the positive background case than in the negative background case. This is indicative of a stronger thermally direct circulation and implied baroclinic energy conversion.

In order to examine the optimality of the SV for changing the quasi-geostrophic forcing, the impact of adding SV1 to the analysis is compared with the impact of adding SV1 to an analysis field for which the SV has not been optimized (i.e. an analysis field from a different day). The impact of adding the fifth SV (SV5) to the analysis is also examined. Figure 12 shows the impact on the Q-vectors (i.e. the Q-vectors of the positive background minus the Q-vectors of the unperturbed background) for these three experiments. The impact on the Q-vector divergence field is also shown*. The impact of SV1 on the Q-vector field (Fig. 12(a)) is of comparable magnitude with the Q-vector field itself (Fig. 11(a)). (Note that the contour interval and vector magnitudes in Fig. 12 are half those in Fig. 11.) The sign of the SV is arbitrary, and the same impact of opposite sign occurs when the SV perturbation is subtracted, rather than added to the analysis. However, when the same SV1 perturbation is added to a background state for which it has not been optimized, in a region of weak horizontal temperature gradients and vertical shear, there is a negligible impact on the Q-vector field (Fig. 12(b)). This illustrates that the large impact on the Q-vector field and implied vertical motions is due to the interaction between the background state and the SV perturbation, not the magnitude of the perturbation itself. However, the impact of the SVs on the Q-vectors is not only a function of the size of the perturbation and its location, but also its structure. SV5 is approximately collocated with SV1 and, by construction, has the same initial-time perturbation energy. However, the impact for SV5 (Fig. 12(c)), which has a nonlinear amplification factor of 8.9 over 48 hours, is considerably smaller than for SV1, which has a nonlinear amplification factor of 13.0. (The singular values of these two perturbations are 13.7 and 10.0 for SV1 and SV5 respectively.) Clearly, different perturbations of the same magnitude, placed in the same region, can have notably different impacts on the background Q-vectors. Only a rough correspondence between the SV amplification factor and the impact on the Q-vectors is expected, as there are other mechanisms for perturbation growth. Despite this caveat, three out of four other case-studies of typical low-level SVs yield similar results.

Most of the energy associated with the optimal perturbation at initial time is localized in the middle-to-lower troposphere, but significant upper-level perturbations are induced very rapidly as the SV evolves, as noted in other studies (e.g. Gelaro *et al.* 1999, 2000). It is plausible that the initial perturbations in the mid-troposphere may induce changes in the upper tropospheric background field through changes to the **Q** field and the implied impact on the quasi-geostrophically forced vertical motion. To study this, the control background and positive background analyses are evolved

* For sufficiently small perturbation size, the Q-vector impact is linear (i.e. when a scaled singular vector is added to a particular background field, the impact structure remains the same and the amplitude is proportional to the scaling factor).

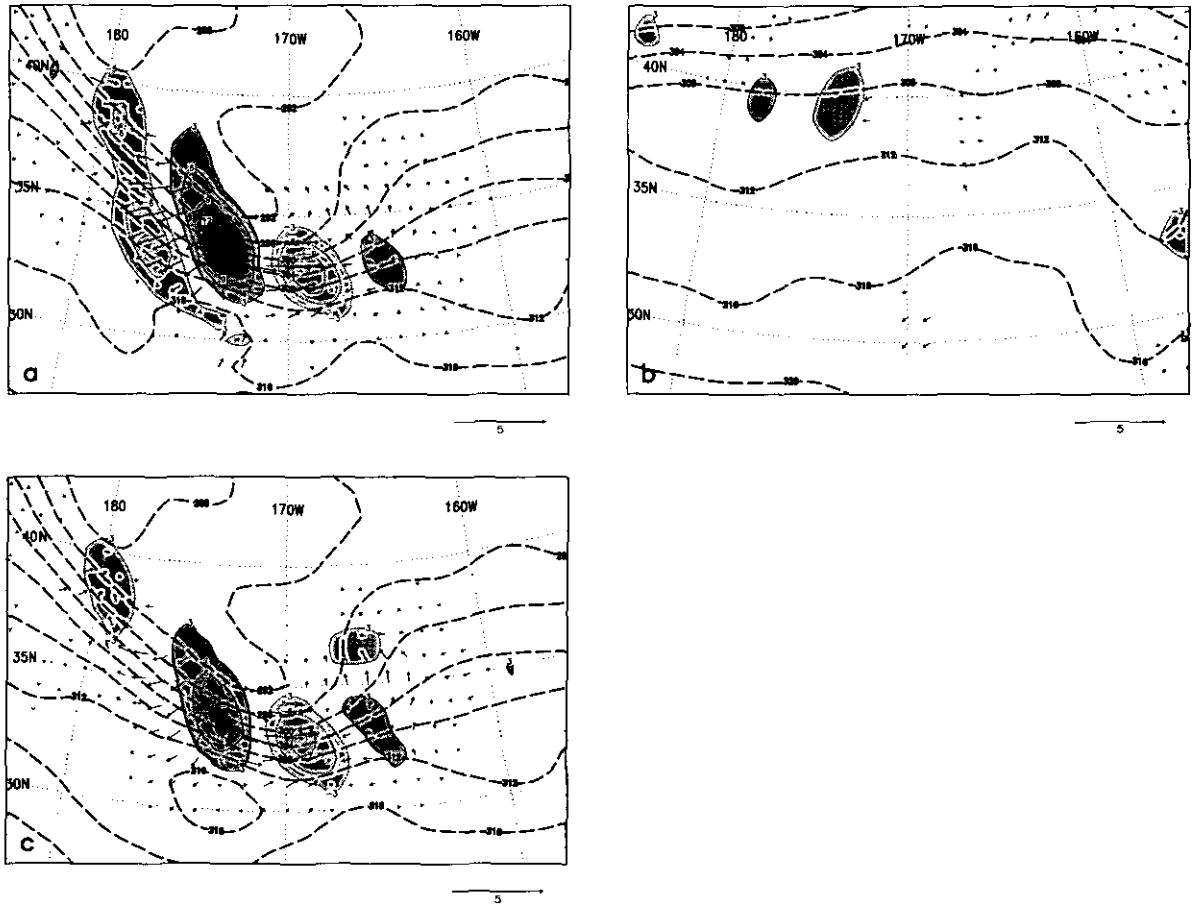

Figure 12. The impact on the Q-vectors (vector scale of 5×10^{-9} K m^{-1}s^{-1}) and Q-vector divergence (shaded, contour interval of 3×10^{-15} K m^{-2}s^{-1} with zero contour omitted) when (a) adding the leading singular vector (SV1) to the appropriate analysis, (b) adding SV1 to an analysis from another day (for which the SV is suboptimal), and (c) adding SV5 to the appropriate analysis. The positive background potential-temperature field is denoted by the thick dashed contours in each panel, (interval of 4 K).

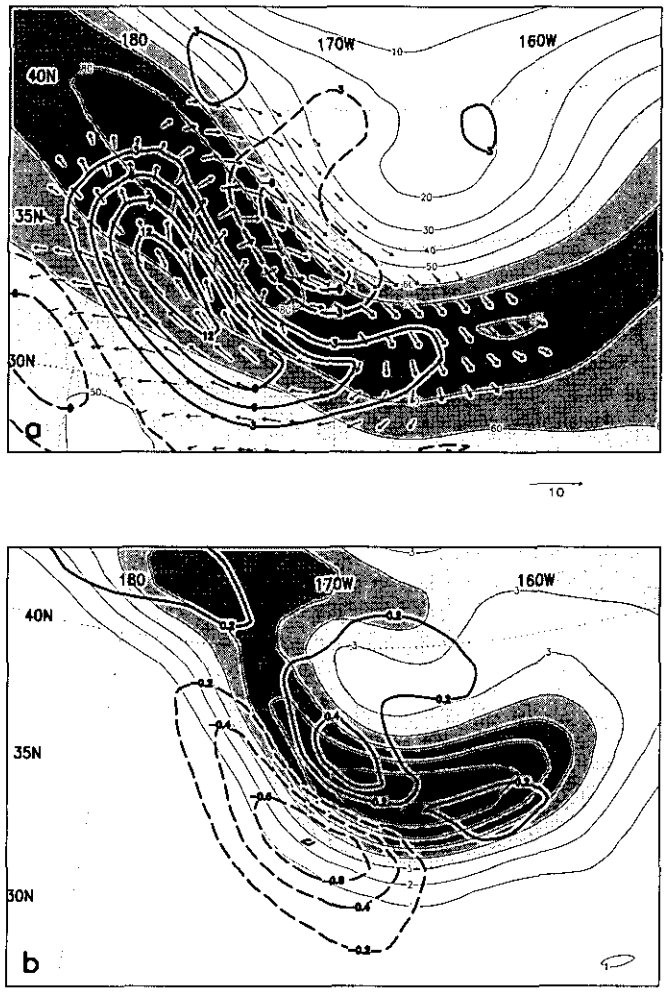

Figure 13. Fields from the 6 h integration: (a) positive background 300 hPa wind speed (shaded, contour interval of 10 m s^{-1}), perturbation vector wind (vector scale of 10 m s^{-1}) and perturbation wind divergence (thick contours, interval of 3×10^{-6} s^{-1}, with zero contour omitted), and (b) positive background 300 hPa potential vorticity (PV) (shading, contour interval of 1 PV unit (PVU)) and perturbation PV (thick contours, interval of 0.2 PVU with zero contour omitted).

using the full nonlinear model, and the evolving perturbations (the differences between the control background and positive background nonlinear integrations) are examined. Figure 13(a) shows the upper-level wind speed and perturbation wind vectors and divergence after 6 hours of model integration. (Note that the wind vectors and divergence contours in Fig. 13 are associated with the perturbation, not the background field itself.) At initial time (not shown), the perturbation wind speed maximum is locally less than 1 m s^{-1}, and the perturbation divergence maximum is locally less than 2×10^{-6} s^{-1} at this level. Just 6 hours later, an upper-level circulation anomaly develops, and the maximum values of divergence are greater than 12×10^{-6} s^{-1}. The upper-level perturbation wind divergence (convergence) occurs over the approximate position of the mid-tropospheric perturbation Q-vector convergence (divergence) and implied upward (downward) motion (Fig. 12(a)). The upper-level perturbation wind across the jet is

TABLE 1. TOTAL, POTENTIAL AND KINETIC ENERGY (J KG^{-1}) FOR THE EVOLVING SINGULAR VECTOR PERTURBATION FROM 24 JANUARY

Hours	Total energy	Potential energy	Kinetic energy
0	1.00	0.62	0.38
6	3.09	0.75	2.34
12	8.44	1.84	6.60
24	32.26	5.52	26.74
48	170.37	28.81	141.56

directed from south-west to north-east, which is consistent with the mid-level thermally direct perturbation circulation implied by the perturbation Q-vectors. Also note that the perturbation temperature anomaly (Fig. 10(a)) is positive in the region of the largest anomalous Q-vector convergence, and negative in the region of the largest anomalous Q-vector divergence, implying baroclinic energy conversion from perturbation potential energy to perturbation kinetic energy. This implied baroclinic energy conversion is consistent with the ratio of perturbation potential and kinetic energy as the perturbation evolves (Table 1). At initial time, potential energy accounts for 62% of the total energy, but increases very little (about 20%) over the next six hours. In contrast, kinetic energy increases by more than a factor of 6, and remains the dominant contribution to the total energy for the reminder of the perturbation evolution.

Figure 13(b) shows the 6 h evolved background 300 hPa PV and perturbation 300 hPa PV. As with the wind field, the PV perturbations at initial time (not shown) are very small at this level. After 6 hours, PV anomalies occur above the mid-level quasi-geostrophic forcing. For the positive SV case, the PV perturbations are such that they enhance the upper-level PV gradient on the southern side of the PV streamer. Beyond 6 hours, the structure of the evolving perturbation becomes considerably more complex. Much more study is needed to understand fully the mechanisms of the rapid perturbation growth in these realistic systems. However, this case-study and others (not shown) clearly illustrate that low- to mid-level SV perturbations can have an important impact on upper-level PV features in a relatively short amount of time.

The 6 h evolved perturbations based on the negative SVs (not shown) are almost perfectly anti-symmetric to the positive SV perturbations shown in Fig. 13. However, nonlinearities become more prominent as integration time increases. While the large-scale features of the perturbations, particularly for smooth fields such as geopotential height, exhibit a significant degree of anti-symmetry out to 48-hours, nonlinear perturbation growth becomes apparent for fields, such as velocity, that have more small-scale structure. Smith and Gilmour (1997) define a linearity test statistic,

$$\Theta = \frac{\|\delta^+(t) + \delta^-(t)\|}{0.5\{\|\delta^+(t)\| + \|\delta^-(t)\|\}},$$

where δ^+ and δ^- represent the positive and negative perturbations, and $\|\|$ represents an appropriate metric. When this test statistic is applied to the positive and negative SV1 perturbations for this case, Θ is 0.14 and 0.38 at 24 and 48 hours, respectively, when measured using the perturbation 200 hPa geopotential height fields. In contrast, when measured using total energy, Θ is 0.39 and 0.99 at 24 and 48 hours, indicating that departures from linearity are of similar magnitude as the perturbations themselves by 48 hours. However, it should be kept in mind that the SV perturbations still evolve very rapidly in the nonlinear system, with nonlinear growth rates similar to the linear growth rates that correspond to the singular values.

(*b*) *Upper-level SVs vs. low-level SVs*

In several case-studies examined, the initial-time SV perturbation occurs below a distinct mid- to upper-level PV feature, propagates upward quickly, and has an impact on that PV feature throughout the forecast evolution. However, as noted previously, not all initial-time leading SVs occur in the middle-to-lower troposphere. In this section, the evolution of a typical, 'low-level' SV (one that has most of its initial-time energy in the lower troposphere) is contrasted with the evolution of an 'upper-level' SV (one that has most of its initial-time energy near 300 hPa). The naming convention refers to their location at initial time only. The examples shown correspond to the leading SVs from 23 January and 18 January 1998.

Figure 14 shows a series of vertical cross-sections of the evolving perturbation total energy (left panels) and perturbation PV (right panels) at the latitude where the perturbation has maximum amplitude. These cross-sections illustrate the evolution of a typical low-level SV at 0 h, 12 h and 48 h integration times (note that the longitude values on the lower axis shift eastward for the 48 h panels). The perturbation total energy is the total energy of the difference field between the control background and positive background integrations (i.e. the difference between the control nonlinear integration and the nonlinear integration to which the SV perturbation has been added at initial time). As before, the PV perturbation fields are the difference fields between the evolving control background and positive background PV fields. The evolving background PV and wind-speed fields associated with the positive background integration are also shown in both the left and right panels.

As with the example shown in the previous subsection, the SV occurs in the lower-middle troposphere at initial time, beneath a depressed region of the tropopause. As it evolves, its influence is quickly seen throughout the depth of the troposphere. The PV difference field shows the fine vertical structure at initial time in the vicinity of strong mid-level vertical shear. As the integration progresses, the PV difference features become 'unshielded' and more elongated in the vertical (as in Badger and Hoskins 2001). These PV difference fields will tend to be larger where the background PV values are larger (e.g. the same vorticity perturbation placed in a region of high static stability will have a bigger impact on the PV than one placed in a region of lower static stability). Thus, even though the perturbation energy extends throughout the depth of the troposphere, the largest PV differences tend to occur where the background PV is largest. Several other case-studies of low-level SV evolution (not shown) exhibit similar behaviour.

Figure 15 is analogous to Fig. 14, but illustrates the evolution of the upper-level SV from 18 January, which serves as a counter example to the typical low-level SV. Unlike the low-level SV, most of the perturbation energy remains in the upper half of the troposphere. The perturbation in this case is not as clearly associated with a distinct upper-level high-PV feature. However, there are some common characteristics between the upper-level and low-level SV evolution. The initial-time PV exhibits significant vertical structure and occurs in a region of upper-level vertical shear. These PV features become 'unshielded' with time as well. Horizontal cross-sections (not shown) reveal an initial tilt into the horizontal shear in both cases, indicating that barotropic energy conversion is probably important as well. The upper-level SV occurs in a region where the latitudinal PV gradient changes sign, also suggesting barotropic instability as a growth mechanism. It is not surprising that the SVs are different, given that they are based on different trajectories. The reason why the leading SV occurs at upper levels at initial time for this case is not clear, but it may be related to the fact that, at final

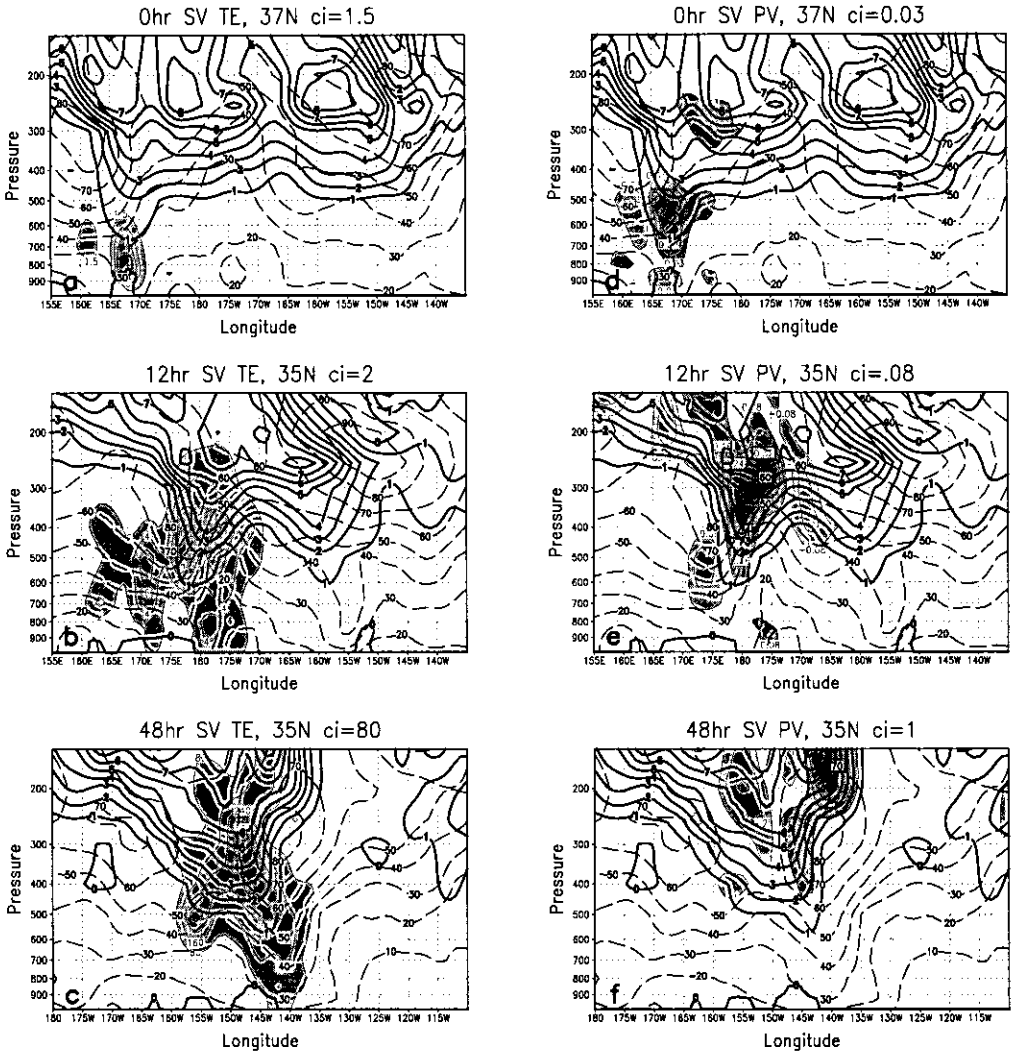

Figure 14. Pressure–longitude plots of the perturbation total energy (left panels) and perturbation potential vorticity (PV) (right panels) for the evolving low-level leading singular vector (SV1) (from 23 January 1998) at (a) and (d) 0 h, (b) and (e) 12 h, and (c) and (f) 48 h. Cross-sections are taken at the latitude of maximum perturbation amplitude. The thick solid contours indicate the background PV field (interval of 1 PV unit (PVU)) and the dashed contours indicate the background wind speed (interval of 10 m s^{-1}). For the left panels, shading indicates perturbation total energy (contour interval (ci) in J kg^{-1} given above each panel). For the right panels, shading indicates the PV perturbation (ci in PVU given above each panel, zero contour omitted).

time, the forecast verification region is almost completely covered by a large ridge and high SLP, (very unusual for this time period). Also, the low-level wind speed below the perturbation is quite weak, and the upper-level initial location might reflect the tendency for the initial-time SV to be located near a steering level (critical level), which would be higher up in the atmosphere for this relatively weak-wind case. This is consistent with initial-time SVs occurring at higher levels in less baroclinic environments such as the tropics or summer-time midlatitudes.

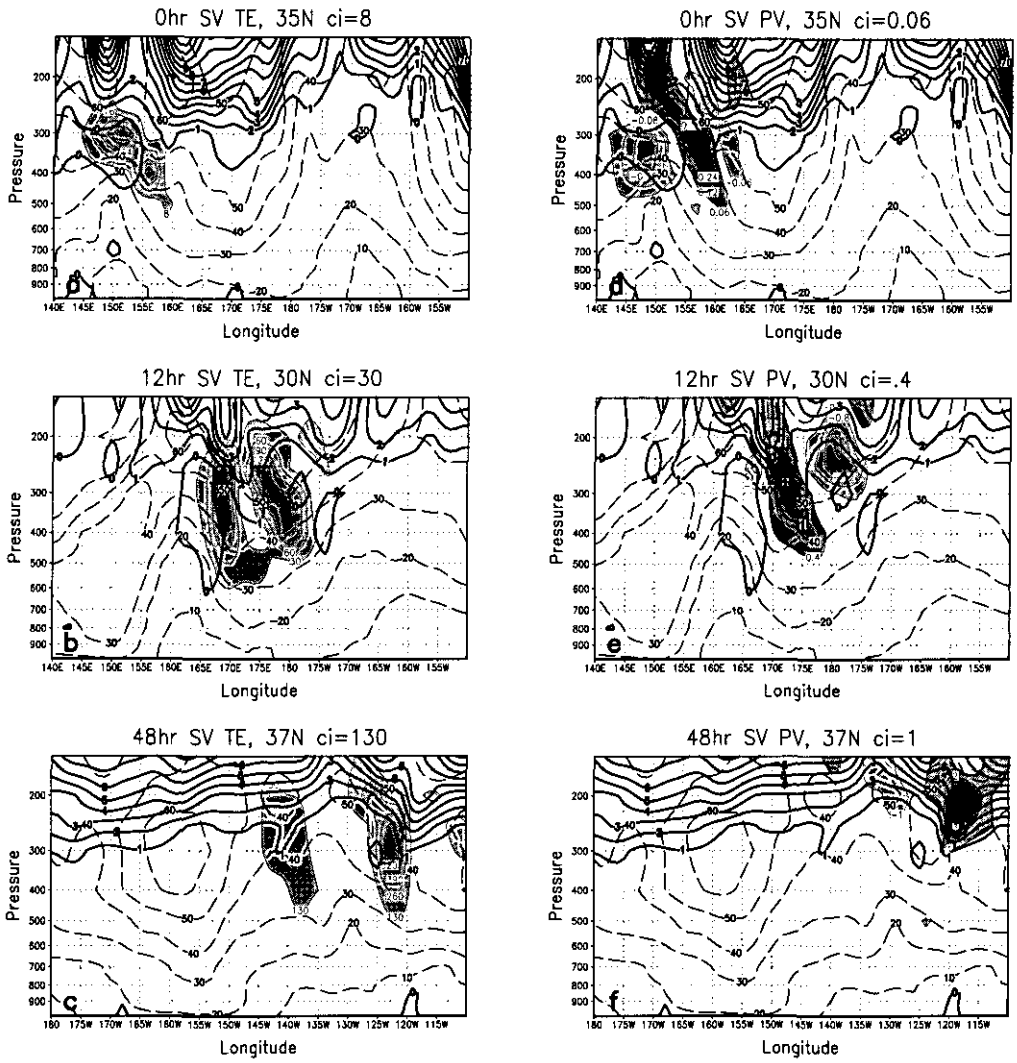

Figure 15. As in Fig. 14, except for the upper-level SV1 from 18 January 1998.

Energy calculations for the perturbation above and below 500 hPa (not shown) confirm that for the typical low-level case most of the perturbation energy starts at low levels, but the energy growth at upper levels is more rapid and overtakes the low-level perturbation energy by 18 hours. On the other hand, most of the energy for the upper-level case remains at upper levels. The perturbation growth rates based on 12-hour intervals, calculated as $\ln(E_2/E_1)^{1/2}/(t_2 - t_1)$, where E_n represents perturbation energy at time n, are given in Table 2. The growth rates decrease during the integration time for both the upper-level and low-level SVs. This decrease is most prominent after the first 12 hours. The upper-level SV growth is faster than the low-level SV growth for the first 12 hours, but after that, the deep perturbation associated with the low-level SV is able to sustain a larger growth rate through the rest of the optimization period. It

TABLE 2. GROWTH RATE (DAY^{-1}) FOR THE LOW-LEVEL AND UPPER-LEVEL SINGULAR VECTOR (SV) PERTURBATIONS

Hours	Low-level SV	Upper-level SV
0–12	1.91	2.38
12–24	1.48	1.28
24–36	1.0	0.68
36–48	0.51	0.32

should be noted that the slower growth rates toward the end of the integration might be caused by nonlinearities in the perturbation evolution.

The finding that the growth rates are larger during the beginning portion of the SV evolution and then drop off with time is consistent with the work of Badger and Hoskins (2001) who show that the initial unshielding phase provides more rapid growth than the secondary phase involving interior PV anomalies and lower-level thermal anomalies. The finding that the upper-level SV does not develop significant low-level perturbations is also consistent with the results of Badger and Hoskins. In their simple model experiments, mid- and low-level initial perturbations are effective in producing a deep impact, while the influence of initial-time upper-level perturbations are mostly confined to the upper levels. This follows naturally from the fact that perturbations configured for upward propagation are tilted against the vertical shear and grow with time. Perturbations configured to propagate downward decay with time as their tilt is enhanced by the shear (Farrell 1984; Reynolds and Palmer 1998; Badger and Hoskins 2001). The results for these case-studies are also consistent with the results of Gelaro *et al.* (2000), who show that initial analysis increments below 400 hPa have a large impact throughout the depth of the troposphere, while analysis increments above 400 hPa have only a small effect on the forecasts at lower tropospheric levels.

Throughout this study the connection between SV perturbations and upper-level PV features has been emphasized. It should be kept in mind, of course, that the SV perturbation energy can propagate away from the PV feature with which it is initially associated. This point is well illustrated by Hovmüller diagrams of the evolving SV 300 hPa meridional wind superimposed on the background 300 hPa PV. Figure 16 shows these Hovmüller diagrams for both the low-level and upper-level SVs of Figs. 14 and 15. Because the latitude of the perturbation maximum is quite variable, the fields are averaged over the latitudinal band from 25°N to 40°N. Meridional wind perturbations are associated with an eastward-moving upper-level trough in both cases. (In the upper-level SV case, Fig. 16(b), the latitudinal averaging obscures the fact that the largest amplitude anomaly occurs equatorward of this upper-level feature.) It takes a few hours for the 300 hPa wind anomalies to appear in the low-level SV case but, after that, the 300 hPa behaviour of the low-level and upper-level SVs is similar. The downstream development ahead of the phase propagation is very clear in both cases. This demonstrates potential problems for targeting observations by tracking upper-level PV features, since forecast errors may, of course, propagate out ahead of individual synoptic features. This issue will become more significant as the optimization time is increased. This effect may well account for the weak composite results at verification time noted in section 3(c).

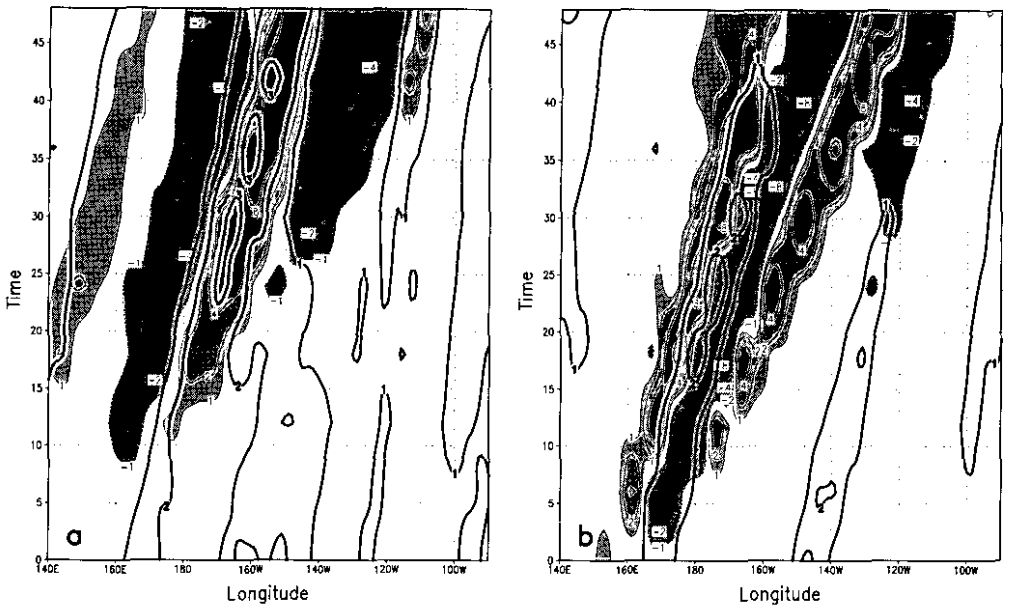

Figure 16. Hovmüller diagrams of the perturbation meridional wind field (shaded, contours at 1, 2, 4 and 8 m s^{-1}) and background potential vorticity (PV) (thick contours, interval of 1 PV unit) at 300 hPa, averaged from 25°N to 40°N, for (a) the 23 January 1998 low-level leading singular vector (SV1) and (b) the 18 January 1998 upper-level SV1.

5. Conclusions

As suggested in previous work (Buizza and Palmer 1995; Palmer *et al.* 1998; Gelaro *et al.* 1999; Morgan 2001), the results of this study confirm that there is often a significant coherent spatial relationship between initial-time total energy SVs and transient features in the background flow, particularly features in the PV field. SVs often occur in regions of enhanced mid-level baroclinicity (enhanced vertical shear and horizontal temperature gradients) and below distinct high-PV features where the tropopause is anomalously low. The composites show that the SVs often occur in dynamically active regions (i.e. regions of significant PV gradients and large quasi-geostrophic forcing), and case-studies indicate that the small perturbations associated with the scaled SVs can have a first-order impact on the Q-vector divergence and implied vertical motion. This mid-level forcing may in turn force significant perturbations at the tropopause level, within the upper-level PV feature.

The results presented here provide evidence that low-level SVs point to the importance of upper-level PV precursor forcing of baroclinic development in many cases. However, the fastest growth occurs during the initial unshielding and upward propagation of energy from the lower-to-middle levels into the middle-to-upper level PV features. Thus, optimal growth is obtained from perturbations that occur below upper-level PV features. This is consistent with the simple model results of Badger and Hoskins (2001) and Morgan (2001), who show rapid growth during the initial stages of unshielding and upward propagation, followed by slower, sustained growth of perturbations that extend throughout the depth of the troposphere.

Although a clear relationship is established between low-level SVs and upper-level PV features, care should be taken when trying to deduce regions of forecast sensitivity

using background PV. As noted here and in other studies, fast-growing perturbations are not always associated with distinct PV features. Also, SV propagation speed is highly variable, and the SVs, of course, can propagate faster than the Lagrangian advection speeds of particular PV features. Hovmüller diagrams of evolving SV perturbations superimposed on background fields (Fig. 16) illustrate this point clearly. It is possible that PV inversion in semi-geostrophic space may be a useful tool for studying the relationship between PV and SVs, as suggested by Xu and Gu (2000), as it is less susceptible to certain limitations of traditional PV diagnosis related to the nonmodality of the development and inadequate resolution.

There are several opportunities for extension of the current research. Although the nonlinear forecast trajectory and evolved perturbations are calculated using the full physics version of the nonlinear model, inclusion of moist physics in the SV calculations may well be significant (see Ehrendorfer *et al.* 1999). It will be very interesting to compare current results with those obtained using a metric that includes moisture. (The moist adjoint of NOGAPS is currently under development.) Also, the use of a stationary local projection operator (rather than one that is placed over a specific system of interest) makes it difficult to generalize some of the results, particularly as they pertain to upper-level SVs. The period of time studied, late January to February 1998 during the El Niño, was typified by enhanced baroclinicity throughout the central and eastern North Pacific, and an anomalously strong Pacific jet, which extended far to the east of the climatological position. Results based on a more typical winter might be different. Investigations of a La Niña winter, as well as other seasons, would be needed to assess both the interannual and seasonal variability of these relationships.

ACKNOWLEDGEMENTS

The authors would like to thank Rolf Langland, Mel Shapiro, Michael Morgan and Jonathan Martin for helpful discussions, and Ron Errico, Istvan Szunyogh, and two anonymous reviewers for helpful reviews of an earlier version of the manuscript. Discussions with Mel Shapiro led to Fig. 16. This research is sponsored by the Naval Research Laboratory and the Office of Naval Research under program element 0601153N, project number BE-033-0345. Partial computing support has been provided by the Department of Defense High Performance Computing Program.

REFERENCES

Appenzeller, C. and Davies, H. C. 1992 Structure of stratospheric intrusions into the troposphere. *Nature*, **358**, 570–572

Badger, J. and Hoskins, B. J. 2001 Simple initial value problems and mechanisms for baroclinic growth. *J. Atmos. Sci.*, **58**, 38–49

Barkmeijer, J. 1992 Local error growth in a barotropic model. *Tellus*, **44A**, 314–323

Bergot, T. 1999 Adaptive observations during FASTEX: A systematic survey of upstream flights. *Q. J. R. Meteorol. Soc.*, **125**, 3271–3298

Borges, M. D. and Hartmann, D. L. 1992 Barotropic instability and optimal perturbations of observed nonzonal flows. *J. Atmos. Sci.*, **48**, 335–354

Boyle, J. S. and Bosart, L. F. 1986 Cyclone–anticyclone couplets over North America. Part II: Analysis of a major cyclone event over the eastern United States. *Mon. Weather Rev.*, **114**, 2432–2465

Buizza, R. 1994 Localization of optimal perturbations using a projection operator. *Q. J. R. Meteorol. Soc.*, **120**, 1647–1681

1998 Impact of horizontal diffusion on T21, T42 and T63 SVs. *J. Atmos. Sci.*, **55**, 1069–1083

Buizza, R. and Montani, A. 1999 Targeting observations using SVs. *J. Atmos. Sci.*, **56**, 2965–2985

Buizza, R. and Palmer, T. N. 1995 The singular-vector structure of the atmospheric global circulation. *J. Atmos. Sci.*, **52**, 1434–1456

Davies, H. C. and Rossa, A. M. 1998 PV frontogenesis and upper-tropospheric fronts. *Mon. Weather Rev.*, **126,** 1528–1539

Demirtas, M. and Thorpe, A. J. 1999 Sensitivity of short-range weather forecasts to local potential vorticity modifications. *Mon. Weather Rev.*, **127,** 922–939

Ehrendorfer, M. and Errico, R. M. 1995 Mesoscale predictability and the spectrum of optimal perturbations. *J. Atmos. Sci.*, **52,** 3475–3500

Ehrendorfer, M., Errico, R. M. and Raeder, K. D. 1999 Singular-vector perturbation growth in a primitive-equation model with moist physics. *J. Atmos. Sci.*, **56,** 1627–1648

Eliassen, A. 1962 On the vertical circulation in frontal zones. *Geofys. Publ.*, **24**(4), 147–160

Errico, R. M. and Vukicevic, T. 1992 Sensitivity analysis using an adjoint of the PSU–NCAR mesoscale model. *Mon. Weather Rev.*, **120,** 1644–1660

Farrell, B. F. 1982 The initial growth of disturbances in a baroclinic flow. *J. Atmos. Sci.*, **39,** 1663–1686

1984 Modal and non-modal baroclinic waves. *J. Atmos. Sci.*, **41,** 668–673

1988 Optimal excitation of neutral Rossby waves. *J. Atmos. Sci.*, **45,** 163–172

1989 Optimal excitation of baroclinic waves. *J. Atmos. Sci.*, **46,** 1193–1206

1990 Small error dynamics and the predictability of atmospheric flows. *J. Atmos. Sci.*, **47,** 2409–2416

Fehlmann, R. and Davies, H. C. 1997 Misforecasts of synoptic systems: Diagnosis via PV retrodiction. *Mon. Weather Rev.*, **125,** 2247–2264

Gelaro, R., Buizza, R., Palmer, T. N. and Klinker, E. 1998 Sensitivity analysis of forecast errors and the construction of optimal perturbations using SVs. *J. Atmos. Sci.*, **55,** 1012–1037

Gelaro, R., Langland, R. H., Rohaly, G. D. and Rosmond, T. E. 1999 An assessment of the SV approach to targeted observations using the FASTEX data set. *Q. J. R. Meteorol. Soc.*, **125,** 3299–3328

Gelaro, R., Reynolds, C. A., Langland, R. H. and Rohaly, G. D. 2000 A predictability study using geostationary satellite wind observations during NORPEX. *Mon. Weather Rev.*, **128,** 3789–3807

Hartmann, D. L., Buizza, R. and Palmer, T. N. 1995 SVs: The effect of spatial scale on linear growth of disturbances. *J. Atmos. Sci.*, **52,** 3885–3894

Hello, G., Lalaurette, F. and Thépaut, J-.N. 2000 Combined use of sensitivity information and observations to improve meteorological forecasts: A feasibility study applied to the 'Christmas storm' case. *Q. J. R. Meteorol. Soc.*, **126,** 621–647

Hogan, T. and Brody, L. 1993 Sensitivity studies of the Navy's global forecast model parameterizations and evaluation of improvements to NOGAPS. *Mon. Weather Rev.*, **121,** 2373–2395

Hoskins, B. J. and Pedder, M. A. 1980 The diagnosis of middle latitude synoptic development. *Q. J. R. Meteorol. Soc.*, **106,** 707–719

Hoskins, B. J. and Valdes, P. J. 1990 On the existence of storm-tracks. *J. Atmos. Sci.*, **47,** 1854–1864

Hoskins, B. J., McIntyre, M. E. and Robertson, A. W. 1985 On the use and significance of isentropic potential vorticity maps. *Q. J. R. Meteorol. Soc.*, **111,** 877–946

Hoskins, B. J., Buizza, R. and Badger, J. 2000 The nature of SV growth and structure. *Q. J. R. Meterol. Soc.*, **126,** 1565–1580

Huo, Z., Zhang, D.-L. and Gyakum, J. R. 1999a Interaction of potential vorticity anomalies in extratropical cyclogenesis. Part I: Static piecewise inversion. *Mon. Weather Rev.*, **127,** 2546–2561

1999b Interaction of potential vorticity anomalies in extratropical cyclogenesis. Part II: Sensitivity to initial perturbations. *Mon. Weather Rev.*, **127,** 2563–2575

Jusem, J. C. and Atlas, R. 1998 Diagnostic evaluation of vertical motion forcing mechanisms by using Q-vector partitioning. *Mon. Weather Rev.*, **126,** 2166–2184

Keyser, D. and Shapiro, M. A. 1986 A review of the structure and dynamics of upper-level frontal zones. *Mon. Weather Rev.*, **114,** 452–499

Lacarra, J.-F. and Talagrand, O. 1988 Short-range evolution of small perturbations in a barotropic model. *Tellus*, **17,** 321–333

Langland, R. H., Elsberry, R. L. and Errico, R. M. 1995 Evaluation of physical processes in an idealized extratropical cyclone using adjoint sensitivity. *Q. J. R. Meteorol. Soc.*, **121,** 1349–1386

Langland, R. H., Gelaro, R., Rohaly, G. D. and Shapiro, M. A.	1999	Targeted observations in FASTEX: Adjoint-based targeting procedures and data impact experiments in IOPs 17 and 18. *Q. J. R. Meteorol. Soc.*, **125,** 3241–3270
Lindzen, R. S. and Farrell, B.	1980	A simple approximate result for the maximum growth rate of baroclinic instabilities. *J. Atmos. Sci.*, **37,** 1648–1654
Lorenz, E. N.	1965	A study of the predictability of a 28-variable atmospheric model. *Tellus*, **17,** 321–333
Martin, J. E.	1999	Quasi-geostrophic forcing of ascent in the occluded sector of cyclones and the trowal airstream. *Mon. Weather Rev.*, **127,** 70–88
Molteni, F. and Palmer, T. N.	1993	Predictability and finite-time instability of the northern winter circulation. *Q. J. R. Meteorol. Soc.*, **119,** 269–298
Molteni, F., Buizza, R., Palmer, T. N. and Petroliagis, T.	1996	The ECMWF ensemble prediction system: Methodology and validation. *Q. J. R. Meteorol. Soc.*, **122,** 73–119
Morgan, M. C.	1999	Using piecewise potential vorticity inversion to diagnose frontogenesis. Part I: A partitioning of the Q vector applied to diagnosing surface frontogenesis and vertical motion. *Mon Weather Rev.*, **127,** 2796–2821
	2001	A potential vorticity and wave activity diagnosis of optimal perturbation evolution. *J. Atmos. Sci.*, in press
Orr, W. McF.	1907	Stability or instability of the steady motions of a perfect liquid. *Proc. R. Irish Acad.*, **27,** 9–69
Palmer, T. N., Gelaro, R., Barkmeijer, J. and Buizza, R.	1998	SVs, metrics and adaptive observations. *J. Atmos. Sci.*, **55,** 633–653
Petterssen, S. and Smebye, S. J.	1971	On the development of extratropical cyclones. *Q. J. R. Meteorol. Soc.*, **97,** 457–482
Pouponneau, B., Ayrault, F., Bergot, T. and Joly, A.	1999	The impact of aircraft data on an Atlantic cyclone analysed in terms of sensitivities and trajectories. *Weather and Forecasting*, **14,** 67–83
Rabier, F., Klinker, E., Courtier, P. and Hollingsworth, A.	1996	Sensitivity of forecast errors to initial conditions. *Q. J. R. Meteorol. Soc.*, **122,** 121–150
Reynolds, C. A. and Palmer, T. N.	1998	The impact of decaying SVs on analysis and forecast correction. *J. Atmos. Sci.*, **55,** 3005–3023
Rosmond, T. E.	1997	'A technical description of the NRL adjoint modeling system'. NRL/MR/7532/97/7230, Naval Research Laboratory, Monterey, CA, 93943-5502 USA
Sawyer, J. S.	1956	The vertical circulation at meteorological fronts and its relation to frontogenesis. *Proc. R. Soc. London*, **A234,** 346–362
Shapiro, M. A., Hampel, T. and Krueger, A. J.	1987	The artic tropopause fold. *Mon. Weather Rev.*, **115,** 444–454
Smith, L. A. and Gilmour, I.	1997	'Accountability and internal consistency in ensemble formation'. Pp. 113–127 in *Predictability Workshop Proceedings*, Reading, United Kingdom, European Centre for Medium-Range Weather Forecasts, UK
Xu, Q. and Gu, W.	2000	Baroclinic Eady wave and fronts. Part II: Geostrophic potential vorticity dynamics in semigeostrophic space. *J. Atmos. Sci.*, **57,** 861–872